Cherenkov Telescope Array sensitivity to the putative millisecond pulsar population responsible for the Galactic Centre excess

Macías, O.; van Leijen, H.; Song, D.; Ando, S.; Horiuchi, S.; Crocker, R.M.

Link to publication

Cherenkov Telescope Array sensitivity to the putative millisecond pulsar population responsible for the Galactic Centre excess

Oscar Macias [ORCID],[1,2]★ Harm van Leijen,[2] Deheng Song [ORCID],[3] Shin'ichiro Ando,[1,2] Shunsaku Horiuchi[3] and Roland M. Crocker [ORCID][4]

[1]*Kavli Institute for the Physics and Mathematics of the Universe (WPI), University of Tokyo, Kashiwa, Chiba 277-8583, Japan*
[2]*GRAPPA Institute, Institute of Physics, University of Amsterdam, NL-1098 XH Amsterdam, the Netherlands*
[3]*Center for Neutrino Physics, Department of Physics, Virginia Tech, Blacksburg, VA 24061, USA*
[4]*Research School of Astronomy and Astrophysics, Australian National University, Canberra, ACT 2611, Australia*

ABSTRACT

The leading explanation of the *Fermi* Galactic Centre γ-ray excess is the extended emission from an unresolved population of millisecond pulsars (MSPs) in the Galactic bulge. Such a population would, along with the prompt γ-rays, also inject large quantities of electrons/positrons ($e^{\pm}$) into the interstellar medium. These $e^{\pm}$ could potentially inverse-Compton (IC) scatter ambient photons into γ-rays that fall within the sensitivity range of the upcoming Cherenkov Telescope Array (CTA). In this article, we examine the detection potential of CTA to this signature by making a realistic estimation of the systematic uncertainties on the Galactic diffuse emission model at TeV-scale γ-ray energies. We forecast that, in the event that $e^{\pm}$ injection spectra are harder than E^{-2}, CTA has the potential to robustly discover the IC signature of a putative Galactic bulge MSP population sufficient to explain the Galactic Centre excess for $e^{\pm}$ injection efficiencies in the range of $\approx$2.9–74.1 per cent, or higher, depending on the level of mismodelling of the Galactic diffuse emission components. On the other hand, for spectra softer than $E^{-2.5}$, a reliable CTA detection would require an unphysically large $e^{\pm}$ injection efficiency of $\gtrsim$158 per cent. However, even this pessimistic conclusion may be avoided in the plausible event that MSP observational and/or modelling uncertainties can be reduced. We further find that, in the event that an IC signal were detected, CTA can successfully discriminate between an MSP and a dark matter origin for the radiating $e^{\pm}$.

Key words: pulsars: general – dark matter – gamma-rays: general.

1 INTRODUCTION

Fermi Large Area Telescope (*Fermi*-LAT) observations (Abazajian 2011; Hooper & Goodenough 2011; Abazajian & Kaplinghat 2012; Gordon & Macias 2013; Macias & Gordon 2014; Calore, Cholis & Weniger 2015; Ajello et al. 2016; Daylan et al. 2016; Ackermann et al. 2017) of the inner $\sim$10° of the Galactic Centre (GC) region have revealed extended γ-ray emission in significant excess with respect to the astrophysical background model. Early studies of this 'GC excess' (GCE) appeared to show the signal to be spherically symmetric around the GC with a radially declining intensity. This, together with the fact that the GCE is described by a spectral energy distribution peaked at a few GeV, led to the possibility that it originates from self-annihilation of weakly interacting massive particles (WIMPs) spatially distributed according to something approaching (actually somewhat steeper than) a Navarro–Frenk–White (NFW) density profile (Hooper & Goodenough 2011; Abazajian & Kaplinghat 2012; Gordon & Macias 2013). However, recent reanalyses of the spatial morphology of the GCE (Bartels et al. 2018; Macias et al. 2018, 2019; Abazajian et al. 2020) have demonstrated that its spatial morphology is better described by the (non-spherically symmetric)

stellar density distribution of the Galactic bulge than by profiles expected for the WIMP annihilation. The Galactic bulge hosts a large variety of stellar populations from old to recently formed (Garzon et al. 1997; Hammersley et al. 2000), and should contain many types of γ-ray sources, the prime example of which is the expected large population of millisecond pulsars (MSPs; Abazajian 2011; Abazajian & Kaplinghat 2012; Gordon & Macias 2013; Ploeg et al. 2017; Fragione, Antonini & Gnedin 2018a; Fragione, Pavlík & Banerjee 2018b; Gonthier et al. 2018; Ploeg et al. 2020) – old pulsars that have been spun-up due to their interaction within a binary system.

In particular, Abazajian et al. (2020) performed a reanalysis of the GCE and demonstrated that, when including maps tracing stellar mass in the Galactic and nuclear bulges, the GC shows no significant detection of a dark matter (DM) annihilation signal. These results were shown to be robust to generous variations of the astrophysical backgrounds [e.g. combinations of two-dimensional (2D) or three-dimensional (3D) inverse-Compton (IC) maps, interstellar gas maps, and a central source of electrons] and DM morphologies (e.g. cored DM profiles, generalized NFW, and ellipsoidal versions of these). This allowed some of us to obtain very strong constraints on DM properties. Interestingly, the key result that the spatial morphology of the GCE is better described by a stellar bulge template than by a NFW model has been recently confirmed by an updated analysis

★ E-mail: o.a.maciasramirez@uva.nl

with SkyFACT (Calore, Donato & Manconi 2021). Though we notice that Di Mauro (2021) obtained otherwise.

Several recent studies (e.g. Bartels, Krishnamurthy & Weniger 2016; Lee et al. 2016; Balaji et al. 2018; Leane & Slatyer 2019; Buschmann et al. 2020; Chang et al. 2020; Leane & Slatyer 2020a, b; Calore et al. 2021) have also proposed different methods to resolve the source nature of the GCE. Although there is no consensus yet in the community regarding the main results of such methods (e.g. Bartels et al. 2016; Balaji et al. 2018; Buschmann et al. 2020; Leane & Slatyer 2020a, b), it should be noted that these studies are probing the photon-count statistics of the GCE, which is an aspect of the signal that is independent of the morphological analyses and results in Macias et al. (2018, 2019) and Bartels et al. (2018). Indeed, the spectrum and spatial morphology are the most basic characteristics of the γ-ray sources in the sky (Abdollahi et al. 2020), and these two characteristics of the GCE are in strong agreement with a Galactic bulge explanation of the GCE (e.g. Abazajian et al. 2020).

Pulsars have long been predicted to be sources of electron–positron ($e^\pm$) pairs (Erber 1966; Sturrock 1970, 1971; Aharonian, Atoyan & Voelk 1995; Atoyan, Aharonian & Völk 1995). Highly energetic $e^\pm$ in the wind regions or inner magnetospheres of pulsars, also when released into the general interstellar medium (ISM), can IC scatter ambient photons to very high energies. The recent HAWC (Abeysekara et al. 2017) observations of extended TeV-scale γ-ray emission around Geminga and Monogem have provided indirect evidence for TeV $e^\pm$ acceleration in normal pulsar nebulae. Since a multitude of normal pulsars have been observed in the vicinity of the Solar system, they have been purported (Hooper, Blasi & Serpico 2009; Delahaye et al. 2010; Abeysekara et al. 2017; Hooper et al. 2017; Profumo et al. 2018; Di Mauro, Manconi & Donato 2019; Jóhannesson, Porter & Moskalenko 2019) as the likely source of the majority of local cosmic ray (CR) positrons (Aguilar et al. 2013). Several lines of evidence also point to potentially efficient $e^\pm$ acceleration by MSPs. First, a recent study (Sudoh, Linden & Beacom 2021) of the correlation between far-infrared (IR) and radio luminosities in star-forming galaxies (SFGs) found that radio emission from MSPs may account for a large fraction of the radio luminosity observed in systems with high stellar mass but low star formation rate. In particular, the unexpectedly high radio luminosities of such systems might be explained by the cooling of GeV-scale $e^\pm$ from MSPs via synchrotron radiation in each host galaxy's ISM. Secondly, Song et al. (2021) have found evidence for IC emission produced by MSP populations in globular clusters of the Milky Way. Furthermore, the H.E.S.S. telescope has observed extended TeV γ-ray emission from the direction of the globular cluster Terzan 5 (Abramowski et al. 2013). Such γ-rays could naturally arise from Comptonization of the background radiation within the globular cluster by super-TeV $e^\pm$ (Bednarek, Sitarek & Sobczak 2016). Note that while a similar search conducted by H.E.S.S in another 15 globular clusters (Abramowski et al. 2013), and MAGIC in the M15 globular cluster (Acciari et al. 2019), only produced γ-ray flux upper limits, it seems likely that forthcoming γ-ray instruments could resolve a large number of globular clusters at TeV energies (Ndiyavala, Krüger & Venter 2018; Ndiyavala-Davids et al. 2020). Thirdly, several analyses of the GCE (e.g. Horiuchi, Kaplinghat & Kwa 2016; Linden et al. 2016; Di Mauro 2021) have found evidence for a high-energy tail, possibly related to IC emission from $e^\pm$ accelerated by the sources responsible for it. Finally, recent simulation work (Guépin, Cerutti & Kotera 2020) suggests that MSPs could efficiently accelerate $e^\pm$ pairs to TeV-scale energies and beyond.

In this paper, we propose that the hypothesized population of approximately 20 to 50 thousand MSPs (Ploeg et al. 2020) in the Galactic bulge could inject large numbers of highly energetic $e^\pm$ into the ISM.[1] The IC signal resulting from these could be detectable (Song, Macias & Horiuchi 2019) by planned TeV-scale γ-ray telescopes such as the Cherenkov Telescope Array (CTA). In particular, CTA will observe the centre of the Milky Way with unprecedented spectral and spatial detail (Acharya et al. 2018). CTA's anticipated strategy for a survey of the inner Galaxy entails a deep exposure observation of the inner few degrees of the GC region plus an extended survey covering a large fraction of the northern side of the Galactic bulge ($|l| \lesssim 6°$ and $0.3° \lesssim b \lesssim 10°$). The latter will facilitate the study of diffuse very high energy (VHE) sources such as Galactic outflows [a possible VHE counterpart to the Fermi bubbles (FBs)], interstellar gas-correlated γ-ray emission, a potential DM emission signature (Acharyya et al. 2021), unresolved γ-ray sources (Viana et al. 2020), and, as we will thoroughly explore here, the IC emission from the population of $e^\pm$ launched into the bulge ISM by the MSPs putatively responsible for the GCE.

Recently, Song et al. (2019) performed detailed simulations (using GALPROP V54; Porter, Moskalenko & Strong 2006) of the IC signature from the putative population of MSPs responsible for the GCE. Compared to that work, here we recompute all our spatial maps using the latest version of the code (GALPROP V56) – which contains new 3D models for the interstellar radiation fields (ISRFs), Galactic structures, and interstellar gas maps. Furthermore, now we run our simulations in the 3D mode of the GALPROP framework, abandoning the assumption of Galactocentric cylindrical symmetry. Interestingly, Song et al. (2019) argued that it could be possible for CTA to (i) detect the population of MSPs responsible for the GCE, and (ii) distinguish whether the IC signal emanates from either DM self-annihilation or these unresolved MSPs in the Galactic bulge.

Here, we perform a realistic assessment of the sensitivity of CTA to such an unresolved population of MSPs in the GC. Using simulated data, we consider scenarios where the Galactic diffuse emission (GDE) is known accurately, as well as cases where the GDE is mismodelled. In each case, we investigate the necessary conditions for a reliable CTA detection of the MSPs' IC signal. Similarly, we study whether CTA could separate the nature of the source producing the IC emission. As shown in Song et al. (2019), the expected IC emission from the Galactic bulge MSPs has morphological differences with respect to the one from DM emission. We now present a systematic study on simulated data that takes into account the latest CTA instrument response function (IRF) and state-of-the-art models for the GDE to fully address these points.

This paper is organized as follows. In Section 2, we describe the procedure used to construct the TeV-scale IC flux maps produced by the putative MSP population responsible for the GCE. In Section 3, we present the astrophysical backgrounds in the GC region that are relevant for the IC searches. In Section 4, we provide an overview of the expected CTA performance, the expected background and signal rates, and the methodology to estimate the CTA sensitivity. We present our results in Section 5, and the discussion and conclusions in Section 6.

---

[1]Note that other studies (e.g. Guépin et al. 2018) have explored the proton signatures from GC MSPs.

2 COMPUTATION OF IC EMISSION FROM MSPS IN THE GC

2.1 Production mechanisms of $e^\pm$ pairs in MSPs

MSPs are neutron stars with high rotation rates (spin periods in the range of tens of ms or less) and relatively low surface magnetic fields ($\sim 10^8$ G). Due to their very rapid rotation, MSPs can produce high electric fields and spin-down power. Despite their low surface magnetic fields, their very compact magnetospheres allow for magnetic fields at the light cylinder that are comparable to those of normal pulsars (Harding 2021). Their observed pulsed emission – as seen by an observer located inside the cone scanned by the magnetic field – is explained by the misalignment of the pulsar rotation axis and the magnetic field axis. If the neutron star surface temperature (T_s) is greater than the electron surface binding temperature (i.e. $T_s \gtrsim 10^5$ K), then electrons can be torn from the neutron star surface by the strong electric fields (Michel 1991). Such electrons would subsequently move parallel to magnetic field lines and emit γ-ray photons through curvature radiation. An additional large number of 'secondary' electrons (and positrons) can be created through pair production processes at different sites throughout the MSP magnetosphere. Dedicated phenomenological studies of MSPs demonstrate that most of their high-energy emission occurs near the current sheet outside the light cylinder (Abdollahi et al. 2020; Harding 2021) Furthermore, in global magnetosphere models, charge currents, electromagnetic fields, and current sheets scale with the light cylinder independent of the pulsar surface magnetic field strength or rotation period. Thus, new emission models of MSPs predict high-energy radiation that is similar to that of normal pulsars (the reader is referred to Harding 2021 for further details).

2.2 Spatial distribution of the MSP population in the GC

A very interesting implication of recent GCE analyses (Bartels et al. 2018; Macias et al. 2018; Macias et al. 2019; Abazajian et al. 2020) is that prompt γ-ray emission from MSPs in the Galactic bulge could account for the bulk of the GCE emission (Abazajian & Kaplinghat 2012). Since prompt emission occurs within or very close to the magnetospheres of individual MSPs and γ-rays travel following geodesics in space–time, the spatial morphology of the GCE can be used to map the spatial distribution of this putative MSP population.

Here, we follow the same approach as Song et al. (2019), who assumed that the MSP population is smoothly distributed following the density of stars in the Galactic bulge (see Section 6.2). In particular, the Galactic bulge consists of two main components: the nuclear bulge and the boxy bulge (see Appendix A, available online). The former corresponds to the stellar structures residing in the inner $\sim$200 pc of the GC [the nuclear stellar disc (NSD) and the nuclear star cluster; Launhardt, Zylka & Mezger 2002], and the latter refers to the stars residing in the inner $\sim$3 kpc of the Galactic bar (Freudenreich 1998; Coleman et al. 2020). However, we also consider the case where the $e^\pm$ sources are distributed with spherical symmetry as this would be spectrally and spatially similar to the IC signal from DM annihilation. More specifically, for the spherical distribution of $e^\pm$ sources we use a generalized NFW profile with a mild radial slope. Detailed descriptions of the stellar density maps and the NFW map used in this work are given in Appendix A (available online).

A potentially relevant effect, which our simulations do not consider, corresponds to the possible smearing effect on the source distribution caused by the MSP kick velocity distribution. However, it is expected that the kicks experienced by MSPs are lower ($\approx$10–

50 km s^{-1}) than those for normal pulsars (Podsiadlowski, Pfahl & Rappaport 2005). This comes mainly from the observation that the escape velocity in globular clusters ($\lesssim$50 km s^{-1}, according to Pfahl, Rappaport & Podsiadlowski 2002) is much lower than the average kick velocity of normal pulsars ($\sim$250 km s^{-1}; Hobbs et al. 2005; Atri et al. 2019), yet globular clusters have been observed to contain a large number of MSPs. For initial kick velocities $\lesssim$20 km s^{-1}, we estimate a negligible smearing of the Galactic bulge stellar density maps. However, we will make a more in-depth investigation of the impact of this effect in a future study of this subject.

2.3 Propagation of CRs in the Galaxy

Given the aforementioned spatial distribution of MSPs in the Galactic bulge, Song et al. (2019) thoroughly studied the injection and propagation of highly energetic $e^\pm$ from MSPs into the ISM. The focus of that study was the construction of high-resolution IC maps for TeV-scale morphological analyses of future γ-ray observations. There, it was shown that while the prompt γ-rays from MSPs trace the γ-ray source distribution, their IC counterpart exhibits an energy-dependent spatial morphology. This is due to the IC emission being the result of the convolution of the relevant photon targets – starlight, IR light, the cosmic microwave background (CMB) – with the steady-state CR distribution, which has itself a spatially dependent spectrum because it is, in turn, the product of the CR source distribution and energy-dependent loss and diffusion processes.

Similar to the approach of Song et al. (2019) and Ishiwata et al. (2020), here, we solve the CR transport equation for MSP-accelerated $e^\pm$ using a customized version of the numerical propagation code GALPROP (Porter et al. 2006; Strong, Moskalenko & Ptuskin 2007). Given a certain CR source distribution, CR injection energy spectrum, and ISM properties, GALPROP makes self-consistent predictions for the spatial distributions and spatially dependent spectra of all CR species. The GALPROP framework includes pure diffusion, convection, diffusive re-acceleration, and energy losses (e.g. in the lepton case: Coulomb scattering, synchrotron, IC scattering, bremsstrahlung, and nuclear collisions).

Song et al. (2019) computed the propagation of $e^\pm$ with GALPROP version 54 (v54). This version of the code makes some simplifying assumptions for the propagation of Galactic CRs. Namely, it assumes galactocentric cylindrical symmetry of the CR halo, 2D ISRF model, and 2D interstellar gas maps. Importantly, it has been pointed out (Porter, Jóhannesson & Moskalenko 2017; Jóhannesson, Porter & Moskalenko 2018) that these assumptions could significantly impact the predictions of IC, and gas-correlated γ-ray emission. In view of this fact, for the present article, we update the IC calculations of Song et al. (2019) by using the latest release of the code [GALPROP v56 (Porter et al. 2017; Jóhannesson et al. 2018)].

Unlike previous versions of this numerical code, GALPROP v56 contains more sophisticated 3D models of the ISRF, neutral hydrogen, and molecular hydrogen gas. Such recent improvements of the code have allowed for detailed predictions of anisotropies (Porter et al. 2017; Jóhannesson et al. 2018) in the Galactic diffuse γ-ray emission and better, physically motivated solutions for the CR transport equation. Currently, there are two alternative 3D ISRF models that are available to the user: The first one is based on the Galaxy model proposed by Freudenreich (1998) (F98), and the second one is based on Robitaille et al. (2012) (R12). Despite that these two models assume different dust densities, and stellar luminosities, their predicted local fluxes are both consistent with near/far-IR measurements. Motivated by previous analyses

Table 1. GALPROP propagation parameter set-up. The parameters (X_h, Y_h, Z_h) and $(\Delta X, \Delta Y, \Delta Z)$ give the size of the CR halo and the spatial resolution (grid size) in Cartesian coordinates, respectively. The diffusion coefficient is a function of rigidity [i.e. $D(R) \propto \beta R^\delta$]. The injection for CR protons is given by $Q(R) \propto R^{\gamma_{0,H}}$ for $R < R_{1,H}$, $Q(R) \propto R^{\gamma_{1,H}}$ for $R_{1,H} < R < R_{2,H}$, and $Q(R) \propto R^{\gamma_{2,H}}$ for $R > R_{2,H}$. Similarly, for CR e^-s it is given by $Q(R) \propto R^{\gamma_{0,e}}$ for $R < R_{1,e}$, $Q(R) \propto R^{\gamma_{1,e}}$ for $R_{1,e} < R < R_{2,e}$, and $Q(R) \propto R^{\gamma_{2,e}}$ for $R > R_{2,e}$. The injection spectrum of heavier CR nuclei is written as $Q(R) \propto R^{\gamma_0}$ for $R < R_1$ and $Q(R) \propto R^{\gamma_1}$ for $R > R_1$. Other parameters included here are the Alfvén velocity ($V_{\text{Alfvén}}$). See Jóhannesson et al. (2018) for more details.

Parameter	Value
X_h (kpc)	± 20.00
Y_h (kpc)	± 20.00
Z_h (kpc)	± 6.00
ΔX (kpc)	0.2
ΔY (kpc)	0.2
ΔZ (kpc)	0.1
$D_{0,xx}$ (10^{28} cm^2 s^{-1})	2.28
δ	0.545
$V_{\text{Alfvén}}$ (km s^{-1})	5.26
γ_0	1.51
γ_1	2.35
R_1 (GV)	3.56
$\gamma_{0,H}$	1.71
$\gamma_{1,H}$	2.35
$\gamma_{2,H}$	2.19
$R_{1,H}$ (GV)	4.81
$R_{2,H}$ (GV)	200
$\gamma_{0,e}$	1.81
$\gamma_{1,e}$	2.77
$\gamma_{2,e}$	2.38
$R_{1,e}$ (GV)	5.97
$R_{2,e}$ (GV)	76

of the GCE (Bartels et al. 2018; Macias et al. 2018, 2019), we limit our study to the F98 Galactic structure model within GALPROP v56.

In this work, we assume a steady-state solution for the CR transport equation, a homogeneous and isotropic diffusion coefficient, allow for diffusive reacceleration, and neglect advection of $e^\pm$ in the Galaxy. All the simulations included in our analysis are performed with the 3D mode of GALPROP. We also adopt the CR source density model labelled as SA50 in Jóhannesson et al. (2018). A brief summary of the main parameter values selected for our analysis is shown in Table 1. Jóhannesson et al. (2018) obtained these propagation parameters following a similar procedure to that presented in Porter et al. (2017). As can be seen in Table 1, for the 3D spatial grid we use a bin size of $200 \times 200 \times 100$ pc^3. Given that nuclear bulge region has a radius of ≈ 200 pc, this spatial resolution is far from ideal for modelling the diffusion processes in this region. However, increasing it further would be very difficult due to very high computing memory demands. We note that our simulations are run in a dedicated computer cluster with 256 gigabytes of memory per node. However, since the code only supports OPENMP environments, it is currently not possible to run fully MPI parallelized simulations.

Given that $e^\pm$ could efficiently lose energy through synchrotron radiation, it is important to select well-motivated parameters for the random magnetic field of the Galaxy. We use the results of a model that matches the 408 MHz synchrotron data (Strong, Moskalenko & Reimer 2000), and that agrees with total magnetic field estimates (Heiles 1995; Beck 2001). In particular, we use the

default double-exponential model included in GALPROP

$$B(r, z) = B_0 \exp\left(-\frac{r - R_\odot}{R_0}\right) \exp\left(-\frac{z}{z_0}\right), \tag{1}$$

where $B_0 = 5$ μG, $R_0 = 10$ kpc, and $z_0 = 2$ kpc. These parameter values are the same as used by Jóhannesson et al. (2018). For the purpose of our current study, we utilize the same random magnetic field parameter set-up in all simulations. However, we note that Song et al. (2019) explored other magnetic field configurations (Crocker et al. 2010) to evaluate their impact on the predicted IC maps.

2.4 Injection luminosity

We assume that the Galactic bulge MSPs are injecting $e^\pm$ at a constant rate into the ISM with a fraction ($f_{e^\pm}$) of their spin-down power ($\dot{E}$) converted into $e^\pm$ pairs. Similarly, the prompt γ-ray luminosity ($L_{\gamma,\text{prompt}}$) is assumed to be proportional to the MSPs' spin-down power, whose efficiency $f_\gamma \equiv L_{\gamma,\text{prompt}}/\dot{E}$ is estimated to be about 10 per cent on average (Abdo et al. 2013). We can hence write

$$L_{e^\pm} = f_{e^\pm}\dot{E} = \frac{f_{e^\pm}}{f_\gamma}L_{\gamma,\text{prompt}} \simeq 10 f_{e^\pm} L_{\gamma,\text{prompt}}, \tag{2}$$

where $L_{e^\pm}$ is the $e^\pm$ injection luminosity. The $e^\pm$ efficiency $f_{e^\pm}$ has been estimated to be between approximately 7 per cent and 29 per cent (computed for $e^\pm$ energies greater than 10 GeV) from TeV observations of normal pulsars (Hooper et al. 2017). Interestingly, a recent phenomenological analysis of MSPs in globular clusters (Song et al. 2021) finds $f_{e^\pm} \approx 10$ per cent, while Sudoh et al. (2021) analysed radio continuum data from galaxies with low specific star formation rates obtaining an MSP $f_{e^\pm}$ that can be even greater than 90 per cent.

In our study, the $f_{e^\pm}$ is estimated using equation (2), simulated GC CTA observations, and the γ-ray luminosity from *Fermi*-LAT observations of the GC. We use the fit results in Macias et al. (2019), which for the boxy bulge obtained $L_{\gamma,\text{prompt}}^{\text{bulge}} = (2.2 \pm 0.4) \times 10^{37}$ erg s^{-1}, and for the nuclear bulge $L_{\gamma,\text{prompt}}^{\text{NB}} = (3.9 \pm 0.5) \times 10^{36}$ erg s^{-1}. A fit that instead of the stellar templates included a DM (NFW^2) template gave a luminosity estimate of $L_{\gamma,\text{prompt}}^{\text{NFW}^2} = (2.7 \pm 0.4) \times 10^{37}$ erg s^{-1}. These two different morphologies are considered in order to investigate the capabilities of CTA to distinguish the two hypotheses under realistic conditions.

2.5 Injection spectrum

For the injection spectrum of the population of GC MSPs, we assume a power law with an exponential cut-off of the form

$$\frac{\text{d}^2N}{\text{d}E\text{d}t} \propto E^{-\Gamma} \exp(-E/E_{\text{cut}}), \tag{3}$$

where Γ is the spectral slope and E_{cut} is the energy cut-off. While in the case of supernova remnants the spectral slope can be constrained from radio measurements, the spectral slope associated with highly energetic $e^\pm$ from pulsars is very difficult to constrain by radio measurements of the pulsed emission (Delahaye et al. 2010). This is due to the fact that the pulsed emission is expected to originate in the polar cap region close to the pulsar magnetosphere, whereas a large portion of the most energetic $e^\pm$ pairs are thought to be accelerated by magnetic reconnection in the equatorial current sheet outside the pulsar light cylinder (Cerutti, Philippov & Spitkovsky 2016). Similarly, the maximum energy that $e^\pm$ can attain from MSPs is very uncertain. The $e^\pm$ pairs produced by MSPs are expected to have much higher energies than those of normal pulsars given that MSPs

Table 2. Injection spectra of $e^{\pm}$ pairs accelerated by a Galactic bulge population of MSPs. See also Song et al. (2019).

Model name	Γ	E_{cut} (TeV)
Baseline	2.0	50
Inj1	1.5	50
Inj2	2.5	50
Inj3	2.0	10
Inj4	2.0	100

have much lower magnetic fields and therefore the pair-producing photons must have higher energies (Harding 2021). Indeed, recent particle-in-cell simulations by Guépin et al. (2020) posit that MSPs could accelerate $e^{\pm}$ pairs even up to PeV energies.

Here, we consider several values that have been explored in the literature (e.g. Yuan & Ioka 2015; Song et al. 2019; Guépin et al. 2020) and that are expected to encompass the range of uncertainties in the energy cut-off and the spectral slope of the MSP injection spectrum. In particular, we select several possible parameter values for Γ, and E_{cut}, as shown in Table 2. Though each individual MSP will surely have a different age, spin-down luminosity, rotation period, magnetic field, and hence a different $e^{\pm}$ injection spectrum, here we assume that the injection spectrum of the whole population of GC MSPs is characterized by a mean injection spectrum (as shown in Table 2).

Using equations (2) and (3), we can obtain the source term $q(\vec{r}, E)$ (with units MeV^{-1} cm^{-2} s^{-2} sr^{-1}) in the CR transport equation to be included to our customized version of GALPROP. Specifically, this can be written as the product of the injection spectrum d^2N/(dEdt) and the MSP density distribution $\rho(\vec{r})$ as follows:

$$q(\vec{r}, E) = \frac{c}{4\pi} N_0 \frac{\mathrm{d}^2 N}{\mathrm{d}E\mathrm{d}t} \rho(\vec{r}), \qquad (4)$$

where the $c/4\pi$ term is a convention in the GALPROP code and N_0 is a normalization factor. We normalize the source function in such a way that its integration over volume and energy matches equation (2):

$$N_0 \int E \frac{\mathrm{d}^2 N}{\mathrm{d}E\mathrm{d}t} \mathrm{d}E \int \rho(\vec{r}) \mathrm{d}r^3 = L_{e^{\pm}}. \qquad (5)$$

This procedure is applied for each injection spectrum described in Table 2, the propagation parameter set-up shown in Table 1, and the spatial distributions given by the stellar mass in the Galactic bulge or DM. Fig. 1 (second and third panels of the bottom row) shows the predicted IC morphology for the Galactic bulge and DM distribution, respectively.

3 BACKGROUND AND FOREGROUND MODELLING

In this section, we describe the different templates used to model the background and foreground emission in the direction of the GC. For this, we use two approaches. First, we make predictions using GALPROP v56. Secondly, we use phenomenological maps whose spectra are extrapolated to match *Fermi*-LAT results. The misidentified CR background is obtained from detailed simulations made publicly available by the CTA consortium.

3.1 Irreducible isotropic γ-ray background

The brightest source of extended γ-ray emission in the direction of the Galactic bulge corresponds to CR protons and e^-s that are misidentified as γ-rays. The interaction of highly energetic CR protons (or heavier nuclei) with the Earth's atmosphere produces showers of neutral hadrons that subsequently decay to γ-rays, an important fraction of which cannot be distinguished from astrophysical γ-rays due to the finite rejection power of CTA (Acharyya et al. 2021; Rinchiuso et al. 2021). Additionally, energetic CR e^-/e^+ induces electromagnetic showers that are very similar to those produced by γ-rays of astrophysical origin.

The main feature of the resulting irreducible γ-ray background is its isotropy. Even though this component is stronger than any other in our region of interest (RoI), the goal is that by using a morphological template fit analysis, the impact of this component can be significantly reduced. We compute the template associated with this background by using dedicated simulation studies performed by the CTA consortium (see Section 4 for details).

3.2 GDE models

The interaction of energetic CRs with interstellar gas, ambient photons, and Galactic magnetic fields produces the brightest source of γ-rays in the *Fermi*-LAT data. This GDE component is very difficult to model due to significant uncertainties in the interstellar gas column density maps, CR spatial/spectral distributions, and the ISRF model.

In this study, we use two different models for the GDE. The first model, referred to as 'GDE model 1', corresponds to one of the representative models constructed in Jóhannesson et al. (2018). The second model, called 'GDE model 2', assumes the hydrodynamic gas maps constructed in Macias et al. (2018), and the IC templates used in Abazajian et al. (2020).

Specifically, 'GDE model 1' assumes the same propagation parameter set-up shown in Table 1, but we note that this model does not include the population of Galactic bulge MSPs that accounts for the GCE. We run GALPROP v56 in its 3D mode, and divide all the predicted TeV-scale γ-ray maps into four Galactocentric rings. Since the bremsstrahlung and hadronic γ-ray maps share the same spatial morphology, we combine these two components into one (gas-correlated γ-ray emission). Dividing the IC/gas-correlated components in different rings allows us to account for the systematic uncertainties associated with the ISM properties and to the somewhat uncertain spatial variation of the CRs. To obtain the flux normalization of each GDE component, we fitted the GALPROP maps to *Fermi*-LAT observations of the inner $15° \times 15°$ of the GC (Macias et al. 2018), separately varying the IC and gas-correlated rings.[2] Fig. 1 (first and second rows) shows the predicted IC, and gas-correlated ring templates at $E = 11.2$ TeV.

For our alternative 'GDE model 2', we use hydrodynamic maps of atomic and molecular hydrogen, in addition to dust residuals tracing dark neutral material. The main motivation of the hydrodynamic method is to reduce biases present in the standard gas maps (Ackermann et al. 2012). In particular, the construction of gas maps requires a model for the gas clouds' velocities in order to obtain their position with respect to the GC. However, the gravitational potential of the Galactic bar induces highly non-circular motion of interstellar gas in the GC region. To overcome this difficulty, while the standard gas maps (Ackermann et al. 2012) generally assume pure circular orbits for the gas, for line-of-sight directions that have $|l| < 15°$ an interpolation method must be used to obtain the gas distribution.

---

[2]This is similar to the method used in Rinchiuso et al. (2021), except that here, the GDE components are divided into different rings.
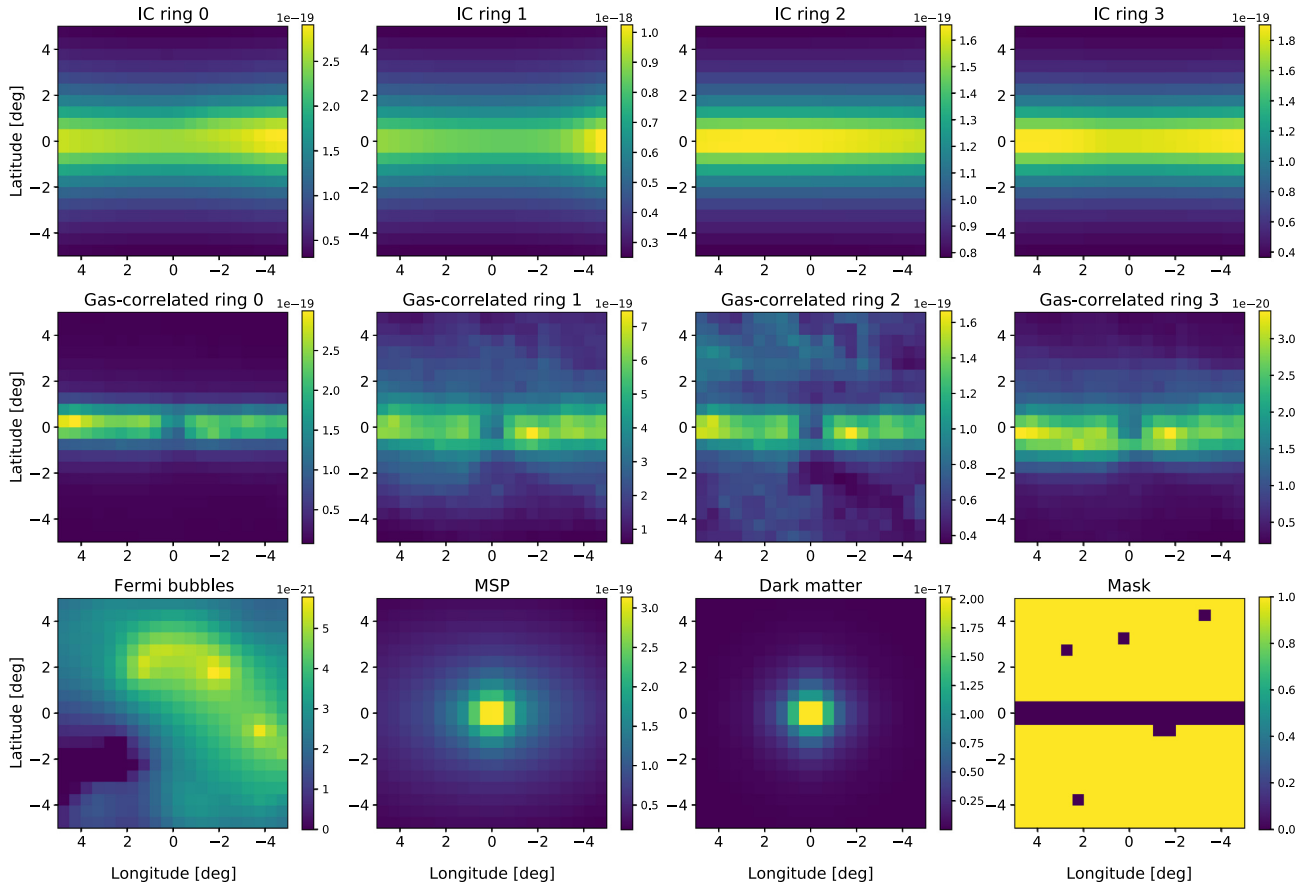
Figure 1. Predicted spatial morphology of various galactic diffusive emission components in the inner $10° \times 10°$ of the Galaxy and at a γ-ray energy of $\approx$11 TeV. All maps are shown in arbitrary units, have a spatial resolution of $0.5° \times 0.5°$, and were computed using GALPROP V56. The top row shows the IC emission produced by background astrophysical sources, which are divided into four Galactocentric rings (0–3.5, 3.5–8.0, 8.0–10.0, and 10.0–50.0 kpc). The middle row shows the gas-correlated γ-ray emission maps (π^0 +bremsstrahlung) also divided into rings of the same size. From left to right, the bottom row shows: the FB template introduced in Macias et al. (2019) (which is based on the one obtained in Ackermann et al. 2014), the predicted MSP IC signal at $\approx$11 TeV, the expected IC signal from a spherical distribution of $e^\pm$ sources also at $\approx$11 TeV (see the text for details), and the mask map, respectively. Note that all the maps in this panel (except for the mask, of course) are normalized to *Fermi*-LAT measurements using the procedure explained in the section corresponding to each map (see also Fig. 3).

Here, instead, we use the hydrodynamic method (Pohl, Englmaier & Bissantz 2008; Macias et al. 2018) that makes direct predictions for the gas velocities in the region $|l| < 15°$, thus providing kinematic resolution in our RoI. Fig. 2 displays all the hydrodynamic templates assumed in this work, which follow the same annular subdivisions of our GALPROP templates (Fig. 1).

Based on detailed statistical tests with *Fermi*-LAT observations of the GC, Macias et al. (2018, 2019) and Buschmann et al. (2020) established that the hydrodynamic maps provide a better fit to the data than the standard gas maps. Although in this article we are introducing these maps with the purpose of estimating the systematic uncertainties in the GDE model, we expect that the hydrodynamic gas maps will be extremely useful once CTA (Acharyya et al. 2021) performs the GC survey.

In order to have a physically motivated spectrum for 'GDE model 2', we assume the same spectra obtained for each ring of the gas-correlated components in 'GDE model 1'. The impact of this assumption in our uncertainties estimates is expected to be small given that the gas-correlated maps have very different spatial morphologies, the templates are divided into rings, and the simulated CTA data are fitted using an analysis procedure that works bin by bin in energy.

3.3 The low-latitude FB template

The FBs are giant γ-ray lobes that were discovered in the *Fermi*-LAT data (Su, Slatyer & Finkbeiner 2010) using template fitting techniques. The FBs stretch out to high latitudes above and below the Galactic plane ($|b| \approx 55°$), while their base (Herold & Malyshev 2019) is positioned slightly offset in longitude from the GC ($l \approx -5°$). They have an approximately uniform intensity, except for the so-called 'cocoon' region in the southern FB lobe (Su & Finkbeiner 2012; Ackermann et al. 2014). At latitudes $|b| \geq 10°$, the FB intensity is well described by a flat power law of the form dN/d$E \propto E^{-2}$, which softens significantly at energies larger than 100 GeV (Ackermann et al. 2014). At latitudes $|b| < 10°$ (Acero et al. 2016; Ackermann et al. 2017; Storm, Weniger & Calore 2017; Herold & Malyshev 2019), the FB spectrum also follows a flat power law but, peculiarly to this region, with no evidence for softening nor an energy cut-off up to energies of approximately 1 TeV.

There is still no consensus on the origin of the FBs. Several possibilities that have been discussed in the literature include recent explosive outbursts (Su et al. 2010) from the supermassive black hole Sgr A*, and sustained nuclear processes (Crocker et al. 2015) such as star formation activity from the GC. These scenarios require
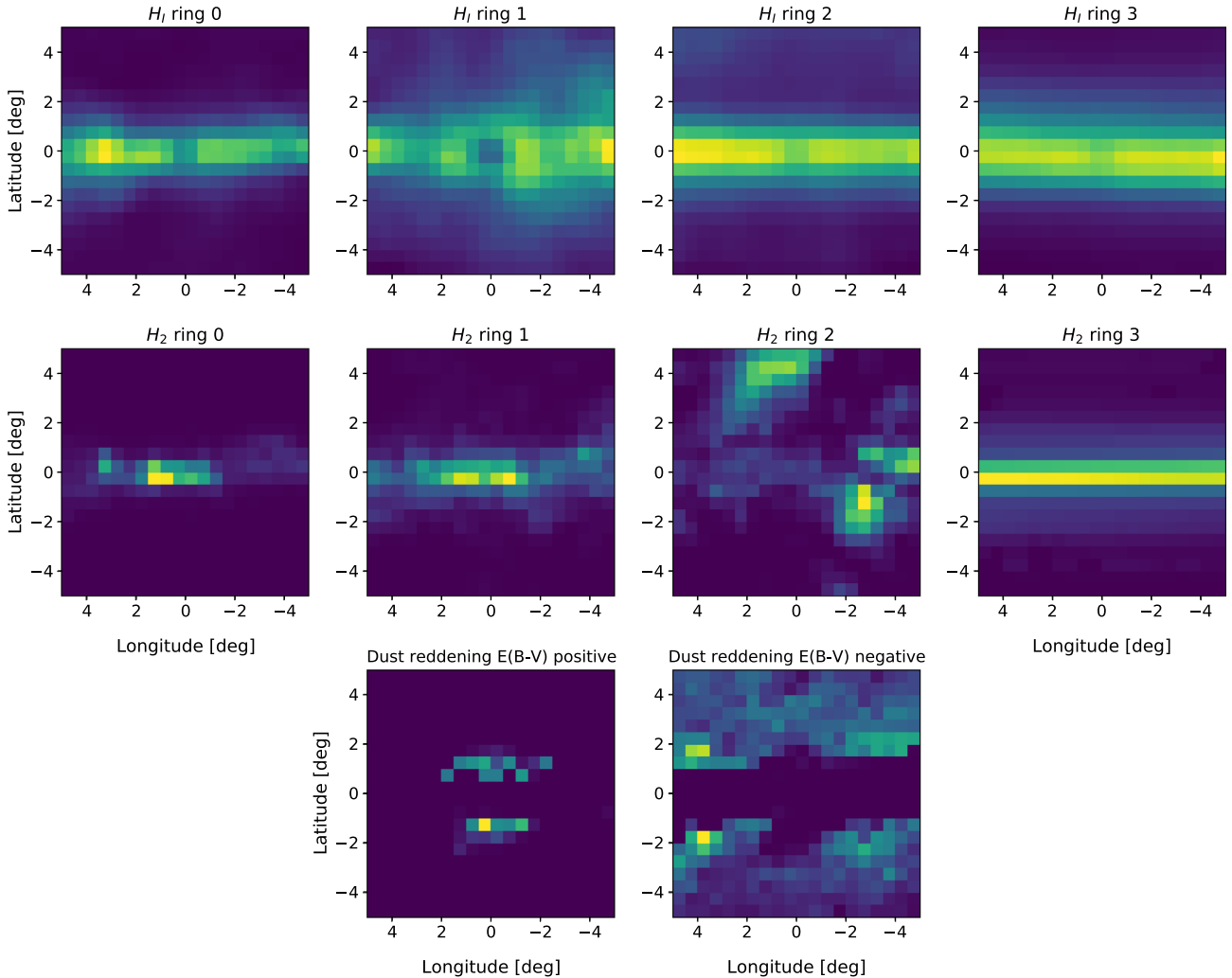
Figure 2. The morphological maps of the gas-correlated γ-ray emission constructed in Macias et al. (2018). The maps are divided into atomic (top panels), molecular hydrogen (middle panels), and residual dust (bottom panels) maps that trace the dark neutral material. The hydrogen maps are divided into the same four Galactocentric rings of Fig. 1.

Table 3. FB models considered in this work. This component is modelled with a power law with exponential cut-off of the form $dN/dE = N_0 (E/1\,\mathrm{TeV})^{-\Gamma} \exp(-E/E_{\mathrm{cut}})$. The model parameters are the same as in Rinchiuso et al. (2021).

Model	N_0 (TeV^{-1} cm^{-2} s^{-1} sr^{-1})	Γ	E_{cut} (TeV)
FB max	1×10^{-8}	1.9	20
FB min	0.5×10^{-8}	1.9	1

either IC or hadronic γ-ray emission to explain the observed spectra.

In this work, we model the FBs using a similar approach to the one used by Rinchiuso et al. (2021). In particular, we assume the best-fitting low-latitude FB spectrum in Ackermann et al. (2017) and then extrapolate it to energies above 1 TeV. We consider two different sets of normalization and energy cut-off, named 'FB min' and 'FB max' (see Table 3). These are chosen such that the FB measurements (Ackermann et al. 2017) fall within the two models, and they do not overshoot the H.E.S.S diffuse observations of the inner $\approx 0.2^\circ$–0.5° of the Galaxy (HESS Collaboration 2016). In

addition, for the spatial morphology of the FBs we use the map obtained by Macias et al. (2019). That analysis used an inpainting method to correct for artefacts introduced by the point source mask in Ackermann et al. (2017). Macias et al. (2019) validated the inpainted FB map with a series of statistical tests. This map is shown in the left bottom corner of Fig. 1.

3.4 Point source and Galactic plane masks

We model the point sources in the RoI following the same approach introduced in Rinchiuso et al. (2021). Namely, we select all the high-energy point sources included in the third *Fermi* high energy catalogue (3FHL; Ajello et al. 2017) that lie within our RoI ($|l| \leq 5^\circ$, $|b| \leq 5^\circ$), and for which the spectrum is given by a simple power law. We note that point sources observed to have an energy cut-off, at GeV-scale energies, in the 3FHL catalogue are not included in our analysis.

Our approach is to mask the aforementioned point sources to avoid potential biases due to extrapolations. We use a disc of radius 0.25° centred at the best-fitting position of each selected 3FHL point

source.[3] In addition, we mask the extended TeV source HESS J1745-303 – one of the brightest sources in our RoI – using a disc of radius $0.4°$. Since the angular resolution of CTA will be smaller than $0.1°$, we anticipate a negligible effect of potential photon leakage. In total, we mask five point sources in our RoI, representing a reduction of approximately 2 per cent of our sky region.

Following Rinchiuso et al. (2021), we mask the Galactic plane region limited by $|b| \leq 0.3°$, which reduces our sky region by an additional ≈ 6.5 per cent. This is to avoid several bright TeV-scale point-like and extended sources in the Galactic plane. Note that even though we mask the Galactic plane, it is still important to include the nuclear bulge map in our GALPROP MSPs simulations. Energetic CR $e^{\pm}$ propagate over much greater distance scales than the size of our plane mask. Our total mask is shown in the bottom right corner of Fig. 1.

4 SENSITIVITY ANALYSIS

We adopt the latest publicly available IRF that is adequate for GC observations (*CTA-Performance-prod3bv1-South-20deg-average-50h.root*[4]). This contains information of the energy-dependent effective area, point spread function, energy resolution, and irreducible γ-ray background (in the energy range 10 GeV–100 TeV). The IRF utilized here was constructed by the CTA team (Hassan et al. 2015) using a suite of dedicated Monte Carlo simulations. These assume an array of detectors composed of 4 large-size telescopes (23 m diameter and sensitive to photons in the 20–150 GeV range), 24 medium-size telescopes (11.5 m diameter and sensitive to the 150 GeV–5 TeV range), and 70 small-size telescopes (4 m diameter and sensitive to the highest energies). At TeV energies, CTA has an energy resolution as good as approximately 5 per cent.

For our analysis, we assume the most favourable observation conditions: a 500 h on-axis observation from the southern site[5] at a mean zenith angle of $20°$. Additionally, we consider events with energies between 16 GeV and 158 TeV. The RoI is selected to be a square of size $10° \times 10°$ – centred at Galactic coordinates $(l, b) = (0°, 0°)$ – which is further binned into pixels of size $0.5° \times 0.5°$. This is the same binning scheme introduced in Rinchiuso et al. (2021). These authors showed that the choice of bin size had no impact on the results given the high photon statistics obtained in each spatial bin. We note that all our background and signal models constructed with GALPROP V56 also have a resolution of $0.5° \times 0.5°$. Increasing the resolution further is limited by computational costs.

4.1 Computation of the expected photon counts

In order to get the expected counts for a given sky model, we convolve the signal/background templates with the CTA IRFs described above. The convolution is done with the GAMMAPY (Deil et al. 2017; Nigro et al. 2019) analysis tools,[6] and the model templates are shown in Figs 1 and 2.

Since the CTA's point spread function is smaller than our pixel size ($0.5° \times 0.5°$), it can be neglected in our calculations. The function that describes the expected counts Φ_{ij}^m for a certain astrophysical

component m, at the i-th longitudinal, j-th latitudinal, and ΔE energy bin, can then be written as

$$\Phi_{ij}^m = T_{\text{obs}} \int_{\Delta E} dE_\gamma \int_0^\infty dE_\gamma' \frac{d\phi_{ij}^m}{dE_\gamma} A_{\text{eff}}^\gamma \left(E_\gamma'\right) D \left(E_\gamma, E_\gamma'\right), \quad (6)$$

where $A_{\text{eff}}^\gamma(E_\gamma)$ is the energy-dependent effective area, $D(E_\gamma, E_\gamma')$ is the energy dispersion function, and $d\phi_{ij}^m/dE_\gamma$ is the incoming flux spectrum from the m source.[7] The whole function is integrated over the energy bin ΔE_γ, and multiplied by the total observation time T_{obs}. The two different energies stand for the true incoming energy E_γ', and the reconstructed energy E_γ. Assuming a homogeneous sky exposure in our RoI, we set $T_{\text{obs}} = 500$ h in our analysis.

As an example of the IRF convolution results, we show in Fig. 3 (left) the predicted spectra for each of the background model components, and in Fig. 3 (right) the same background templates after convolution with the CTA IRFs. We have carefully checked that our pipeline reproduces well previous works in the literature (e.g. Rinchiuso et al. 2021).

4.2 Template fitting procedure

The conventional analysis method for TeV-scale γ-ray observations involves selecting two regions of the sky with approximately the same backgrounds, but different expected signals. The region with larger signal is called the 'ON' region, while the other the 'OFF' region. In this approach, the hypothesis testing is done using a test statistic (TS) defined as the difference in photon counts between the ON and OFF regions. However, the study by Silverwood et al. (2015) demonstrated that the template fitting procedure – which is the standard analysis method for, e.g. the *Fermi*-LAT data – greatly improves the CTA sensitivity to extended GC signals because it allows for the full exploitation of the morphological differences between background and signal templates.

In this work, we adopt a template-fitting approach to study CTA sensitivities to a putative IC signal from Galactic bulge MSPs. In particular, we divide the mock data in 11 bins logarithmically spaced from 16 GeV to 158 TeV. This makes the bins larger than the energy resolution of the CTA data. For each independent energy bin ΔE, we define the likelihood function as

$$\mathcal{L}(\boldsymbol{\mu}|\boldsymbol{n}) = \prod_{ij} \frac{\mu_{ij}^{n_{ij}} e^{-\mu_{ij}}}{n_{ij}!}, \quad (7)$$

where $\boldsymbol{n} = \{n_{ij}\}$ is the simulated data, and the model $\boldsymbol{\mu} = \{\mu_{ij}\}$ is a linear combination of model templates

$$\mu_{ij}(\boldsymbol{\alpha}) = \sum_m \alpha_m \Phi_{ij}^m, \quad (8)$$

with Φ_{ij}^m as given in equation (6), and the flux normalizations α_m are the fitting parameters. The optimization is done with the MINUIT (Nelder & Mead 1965) algorithm contained in the iminuit package.[8]

For each independent energy bin, we simultaneously fit the flux normalizations of all the background and signal components within our $10° \times 10°$ and $|b| \geq 0.3°$ RoI. The normalizations of the sources considered are insensitive to the spectral shape assumed at each energy bin due to the bins being small. This fitting approach, also known as a bin-by-bin analysis, has been widely used in the analysis

---

[3]Note that the $0.25°$ masks end up being just 1 pixel mask due to the low resolution of the other astrophysical maps.
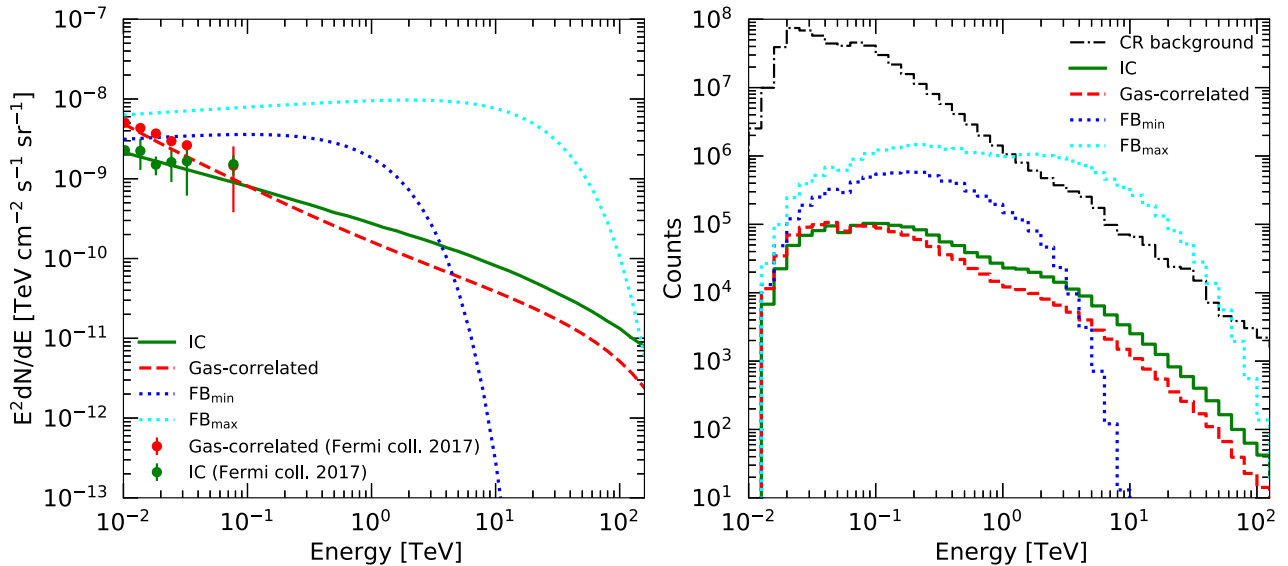
[4]http://cta.irap.omp.eu/ctools/users/user_manual/response.html

[5]This could be obtained with an optimized observation strategy planned by the CTA consortium (Acharyya et al. 2021).

[6]https://gammapy.org/

[7]The irreducible CR background is formally included as an additional component m in equation (6).

[8]https://iminuit.readthedocs.io/en/stable/

Figure 3. The predicted γ-ray spectra for various GDE components and their corresponding CTA count rates for 500 h of observations of the inner $10° \times 10°$ of the GC region. The left-hand panel displays the bin-by-bin fluxes of the IC (green points) and gas-correlated (red points) components of the GDE measured by *Fermi*-LAT (Ackermann et al. 2017). The green solid and red dashed lines are the spectra predicted by GALPROP V56. These are normalized to match the *Fermi*-LAT observations at GeV-scale energies. The blue dotted line corresponds to the best-fitting low-latitude FB spectra in Ackermann et al. (2017) extrapolated to higher energies (this is our FB$_{min}$ model in Table 3). The cyan dotted line is the maximum possible emission that the FBs can take at TeV-scale energy [FB$_{max}$ model in Table 3 – this is the same as in fig. 1 of Rinchiuso et al. (2021)]. The right plot shows the result of convolving the GDE components in the left-hand panel with the CTA IRFs. The irreducible CR background (CR background) is also shown; see Section 4.1 for details.

of the *Fermi*-LAT data (e.g. Ackermann et al. 2015). The advantage of this method over the more traditional broad-band analysis (e.g. Acharyya et al. 2021; Rinchiuso et al. 2021) is that the bin-by-bin method is much less affected by assumptions about the spectral shape of the model templates.

Since CTA is not in operation yet, we create synthetic data for each energy bin and each component. We do this by drawing from a Poisson distribution with mean $\mu_{ij}(\alpha_m)$, and then summing the resulting maps to obtain the total mock data set for an energy bin.

We evaluate the significance of the MSP hypothesis at each energy bin ΔE_k using a TS defined as

$$\mathrm{TS_k} = -2\ln\left(\frac{\mathcal{L}(\boldsymbol{\mu_0}, \hat{\boldsymbol{\theta}}|\boldsymbol{n})}{\mathcal{L}(\hat{\boldsymbol{\mu}}, \hat{\boldsymbol{\theta}}|\boldsymbol{n})}\right), \qquad (9)$$

where $\boldsymbol{\mu_0}$ are the normalizations of the background-only hypothesis, and $\hat{\boldsymbol{\mu}}$ and $\hat{\boldsymbol{\theta}}$ are the best-fitting parameters under the background plus MSPs hypothesis. The total TS of the MSPs IC template can be obtained as $\mathrm{TS} = \sum_{k=1}^{n} \mathrm{TS}_k$, where TS_k is given in equation (9), and the sum runs up to $n = 11$ (number of energy bins). In our case, the MSP IC template has 11 deg of freedom (flux norm at each energy bin). Hence, in order to get the *p*-value of this template we are required to use the mixture distribution formula (Macias et al. 2018)

$$p(\mathrm{TS}) = 2^{-n}\left(\delta(\mathrm{TS}) + \sum_{k=1}^{n}\binom{n}{k}\chi_k^2(\mathrm{TS})\right), \qquad (10)$$

where $\binom{n}{k}$ is the binomial coefficient with $n = 11$, δ is the Dirac delta function, and χ_k^2 is a χ^2 distribution with k degrees of freedom. We can compute the detection significance in σ units corresponding to the addition of one new MSP IC norm parameter by using the total TS value and the *p*-value shown in the above equation. Specifically,

we do this with the following recipe (Macias et al. 2018):

$$\text{Number of } \sigma \equiv \sqrt{\mathrm{InverseCDF}\left(\chi_1^2, \mathrm{CDF}\left[p(\mathrm{TS}), \hat{\mathrm{TS}}\right]\right)}, \qquad (11)$$

where (InverseCDF) CDF is the (inverse) cumulative distribution. The first argument of each of these functions is the distribution function and the second is the value (InverseCDF) at which the CDF is evaluated. The total TS value is denoted by $\hat{\mathrm{TS}}$. From equation (11), we obtain that a 5σ detection corresponds to TS = 41.1. It follows that we may claim a detection of the IC template for total TS values larger than this threshold value.

5 RESULTS

Having introduced the fitting procedure and explained how we create the CTA simulated data, we now present the results of our CTA sensitivity analysis. Specifically, we start by working out the number of independent gas-correlated rings for which we can get stable fits for the background only hypothesis. Then, we present the minimum IC (and $e^{\pm}$) luminosities necessary for a reliable MSP signal detection, and the ability of the method to accurately distinguish between the MSPs and DM origin of the radiating $e^{\pm}$. Finally, we show the impact of the GDE model uncertainties on our results.

5.1 Validation of the GDE model on simulated CTA data

To the best of our knowledge, this is the first time that a Galactic diffuse background model divided into multiple galactocentric rings (see Fig. 1) is used for TeV-scale γ-ray analyses. Though this method has been implemented with great success in studies of the *Fermi* data (e.g. Abdollahi et al. 2020), it is not a priori obvious that the same technique can be applied to CTA, given its smaller field of view.

FB$_{min}$, Perfect GDE
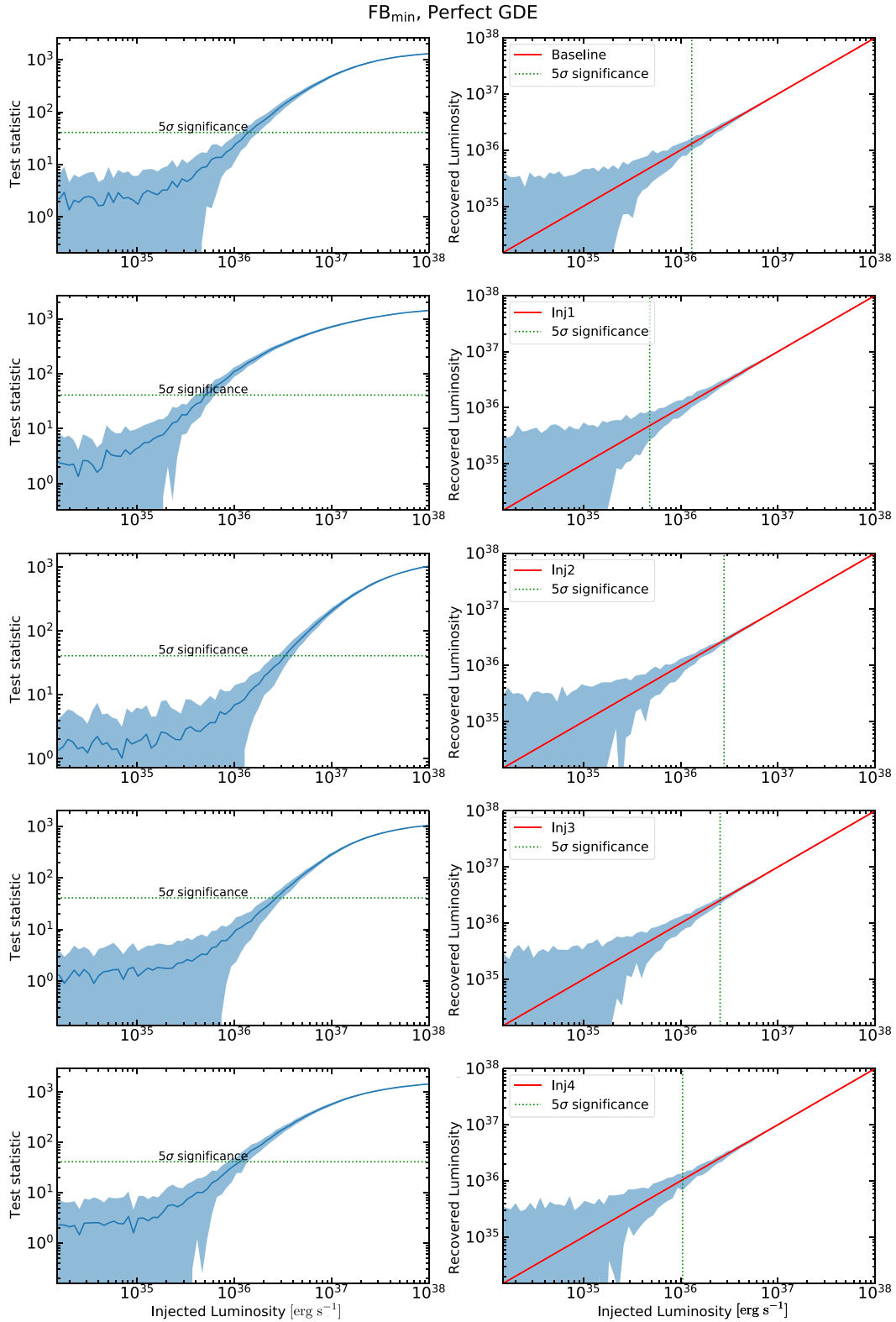
Figure 4. The CTA sensitivity to the IC signal from an unresolved population of MSPs tracing the distribution of stellar matter in the Galactic bulge. These tests assume a perfect knowledge of the GDE. The latter is modelled with a combination of the FB$_{min}$ model and 'GDE model 1' (see also Section 3.2). Left-hand panels: Detection significance (TS) of the MSPs' IC signal for a given IC injection luminosity. Each row assumes a different $e^{\pm}$ spectrum model (Inj1,..., Inj4) shown in Table 2. The 5σ detection threshold is displayed as a green dotted line (see equations 10 and 11) for details. A summary of the minimum $L_{\gamma,IC}$ required for a CTA detection is shown in Table 4. The blue solid line represents the mean of the results, while the light blue region gives its variance. Right-hand panels: Comparison of the recovered signal luminosity with the injected one. The diagonal red line represents the ideal case in which the extracted signal matches the injected signal perfectly. The blue region shows the recovered IC signals. We used 5000 realizations of synthetic data that contain irreducible CR background photons plus astrophysical γ-rays sampled from the aforementioned diffuse model.

FB$_{min}$, Perfect GDE
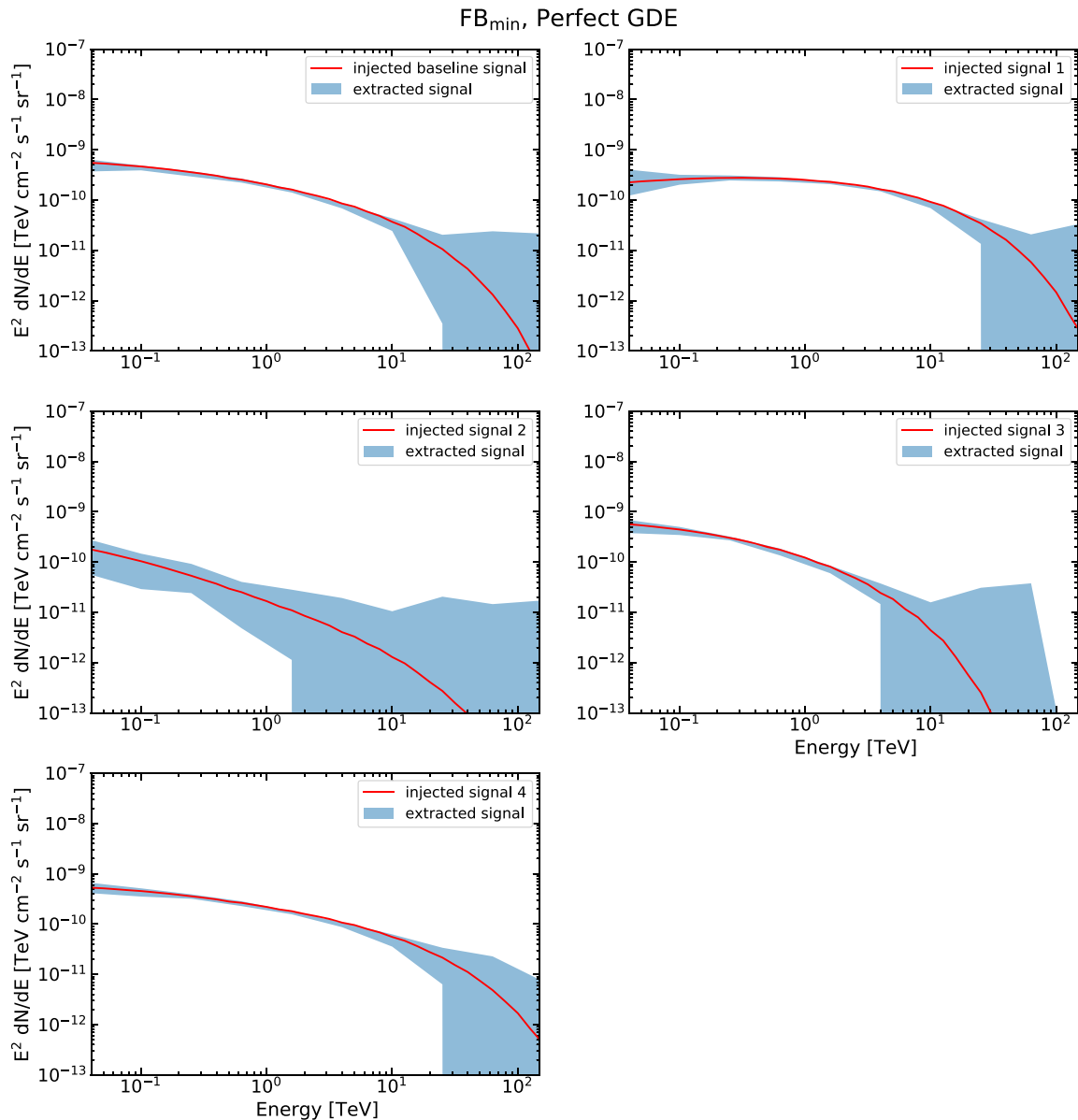
Figure 5. Minimum flux to detect the IC signal from a putative population of MSPs responsible for the GCE. The red line shows the injected IC signal, while the blue regions display the 68 per cent confidence intervals on the recovered signal. The normalization of the spectra corresponds to the γ-ray luminosity that would be detected with 5σ significance (see also the green dotted line in Fig. 4) for 500 h of CTA observations of the central $10° \times 10°$ and $|b| \geq 0.3°$ of the Galaxy. Higher fluxes than the ones displayed here would be detected by CTA with a statistical significance larger than 5σ.

To address this concern, we performed a fitting procedure where we carefully checked for potential degeneracies between the different gas-correlated and IC rings shown in Fig. 1. From this test, we obtained that the morphological differences between the four galactocentric IC emission maps were not significant enough for the pipeline to distinguish them in the simulated data. This is because most of these spatial differences lie in the parts that are further away from our RoI (central $10° \times 10°$ and $|b| \geq 0.3°$ of the Galaxy). We therefore decided to combine the four IC rings into one single map and only keep the gas-correlated emission maps split into four galactocentric rings.

It is worth noting that using different IC rings for GC analyses could still be viable with a different observational strategy. In particular, the GC survey plan proposed in fig. 1 of Acharyya et al.

(2021) covers a region that is almost two times larger than the RoI assumed in our work. Another interesting possibility could be to use the CTA divergent pointing mode (Gérard 2016) in which CTA can survey a region as large as $20° \times 20°$ [see for example the 'Deep exposure scenario' proposed in Coronado-Blázquez et al. (2021)]. We leave these interesting alternatives for future studies, and stick only with our survey strategy, which was suggested in Rinchiuso et al. (2021).

5.2 Sensitivity to the IC signal produced by an unresolved population of MSPs in the GC

Given that the systematic uncertainties in the GDE model are one of the most difficult problems for GeV-scale γ-ray analyses

of the GC, it is reasonable to assume that this component will also be very challenging for forthcoming CTA observations of similar sky regions. With this in mind, we started our sensitivity analysis by testing how well our pipeline recovers the properties of the simulated MSP IC signal in different case scenarios. In particular, we considered various alternative GDE models, different signal spectra and spatial morphologies, and we further employed a method to study the impact of mismodelling the Galactic diffuse backgrounds. Details of each of our GDE model components are given in Section 3. As for the MSP IC signal, we considered a range of physically reasonable injection spectra presented in Table 2.

Fig. 4 shows the results of our signal recovery tests in the case where the diffuse model is given by 'GDE model 1' plus FB$_{min}$, and we assume that the backgrounds are perfectly modelled; this is accomplished by fitting the mock data with the same templates used in the generation of the simulations. This figure is made from 5000 realizations of synthetic data that contain irreducible CR background photons plus astrophysical γ-rays sampled from the aforementioned diffuse model. Each row corresponds to the five different injection models introduced in Table 2. The luminosity of the signal that is injected (red solid line) is displayed along with the 68 per cent containment on the recovered luminosity (blue region) in the right-hand side panels. We also include the 5σ (TS = 41.1 for 11 degrees of freedom) detection threshold (green dotted line), representing the luminosity above which CTA would reliably detect the IC signal from the putative MSP population in the GC. As can be seen, the injected signal is successfully recovered for luminosities above that in the detection threshold. Below this threshold, the uncertainty on the recovered γ-ray luminosity increases very similarly for all the injection models that were included (see Table 2).

In the left-hand panels of Fig. 4, we present the TS distributions of the signal templates. We stress that while fitting the mock data we allow all components (background and signal templates) to vary in the fits. The filled regions denote the TS distributions of the MSPs' IC signal (light blue) and their mean value (blue solid line) is also displayed. These demonstrate that with 500 h of GC (central $10° \times 10°$ and $|b| \geq 0.3°$ of the Galaxy) observations with the CTA and an accurate knowledge of the astrophysical backgrounds (corresponding to the most optimistic scenario considered in this work) the technique presented here should be able to detect the IC signal from the putative GC MSP population, thereby allowing us to constrain the source populations generating the high-energy γ-rays in this sky region.

For this same case scenario, we present details of the recovered spectra in Fig. 5. Each panel in this figure shows the characteristics of the spectra that are recovered with a 5σ detection significance. The five different panels correspond to each $e^{\pm}$ injection model presented in Table 2. As explained in Section 2, we propagate such $e^{\pm}$ within the GALPROP V56 framework, then produce IC spectral templates (red solid lines), and lastly inject these signal maps into the simulated data. We obtained the results in this figure by fitting the mock data with a bin-by-bin fitting procedure that allows us to work out the fluxes and corresponding 68 per cent confidence intervals (blue filled regions) at each independent energy bin. Fluxes larger than those shown in these panels should be successfully detected by CTA, provided the parent $e^{\pm}$'s are injected by an unresolved population of MSPs (tracing the distribution of stellar mass in the Galactic bulge) and the Galactic diffuse background is perfectly modelled. We also present a summary of the minimum $L_{\gamma,\mathrm{IC}}$ (and $L_{e^{\pm}}$) required for a CTA detection in Table 4.

Table 4. Minimum IC luminosity required for a 5σ significance detection with CTA. The luminosities are computed in the energy range 16 GeV and 158 TeV. The columns correspond to different MSPs $e^{\pm}$ spectra considered in Table 2. The corresponding minimum $L_{e^{\pm}}$ can be obtained by realizing that the $L_{e^{\pm}}/L_{\gamma,\mathrm{IC}}$ ratios are: 21.0 for the *baseline* injection model, 14.3 for *inj1*, 124.7 for *inj2*, 23.4 for *inj3*, and 21.1 for *inj4*. See also Section 6.1 for details. For the computation of the efficiencies, we assumed energies greater than 700 MeV.

Minimum $L_{\gamma,\mathrm{IC}}$ for detection (erg s^{-1})				
Baseline	Inj1	Inj2	Inj3	Inj4
FB$_{min}$, perfect GDE.				
1.3×10^{36}	5.4×10^{35}	3.3×10^{36}	2.7×10^{36}	1.0×10^{36}
FB$_{min}$, mismodelling of the GDE.				
1.8×10^{36}	7.2×10^{35}	3.4×10^{36}	2.8×10^{36}	1.3×10^{36}
FB$_{max}$, perfect GDE.				
7.1×10^{36}	7.5×10^{36}	5.4×10^{36}	6.1×10^{36}	7.2×10^{36}
FB$_{max}$, mismodelling of the GDE.				
9.0×10^{36}	9.4×10^{36}	6.8×10^{36}	7.8×10^{36}	9.1×10^{36}

### 5.3 Tests for degeneracies between the IC maps from MSPs and DM in the GC

In the previous section (Section 5.2), we created mock data by sampling from the 'GDE model 1', FB$_{min}$, and the irreducible CR background. We then injected various different MSP IC signals into the data and applied a fitting procedure to recover the injected signals. In particular, the fit included all the templates used in the generation of the mock data.

In this subsection, we applied the same pipeline, except that this time we also added to the fit an IC template generated by DM emission. Namely, we injected an MSP IC signal into the mock data, and subsequently attempted to recover it by including both the MSP IC and DM IC templates in the fit. The main objective of this test is to figure out the conditions under which CTA would be able to disentangle a new extended γ-ray source in the GC based on the morphological characteristics of the IC radiation emitted by the source.

We present the results of the tests for degeneracy between these two competing hypotheses in Fig. 6. The left-hand panel shows the TS distribution of the DM IC template as a function of the injected MSP IC luminosity. In this panel, we display the mean TS values (green solid line) and their respective 68 per cent containment band (green filled region). As can be seen, for all the evaluated luminosities, the DM IC template was found to have TS $\lesssim 10$ (or a statistical significance of $\lesssim 1.6\sigma$ for 11 degrees of freedom). The right-hand panel shows the injected MSP IC luminosity versus the luminosities recovered for the MSP IC (blue filled region) and the DM IC (green filled region) templates, respectively. It is clear that for IC luminosities larger than the minimum L_γ's given in Table 4 (see the row corresponding to FB$_{min}$, mismodelling of the GDE), only a small fraction of the injected MSP IC luminosity is absorbed by the DM IC template.

5.4 Mismodelling of the GDE

Due to uncertainties in the Galactic diffuse background, it will be challenging for future analyses of actual CTA data to model this component perfectly (Acharyya et al. 2021). We recreate this real-world situation by constructing simulated data with 'GDE model 1' and analysing it with 'GDE model 2', which allows us to test

FB$_{\text{min}}$, Perfect GDE
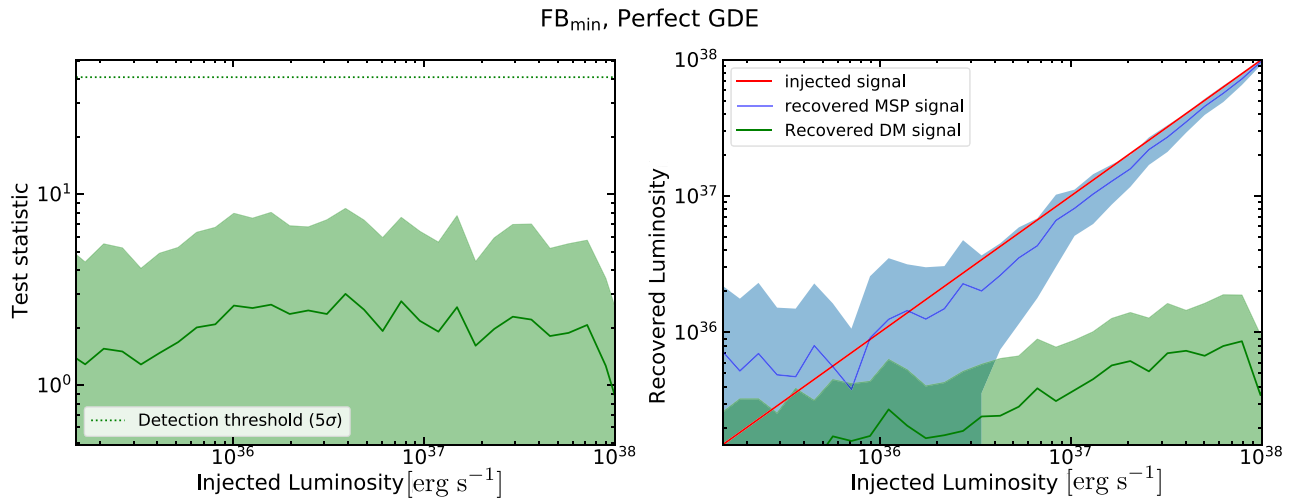
Figure 6. Tests of spectro-morphological degeneracies between the MSP IC and DM IC templates with simulated CTA observations of the GC region. The astrophysical background is sampled from 'GDE model 1', FB$_{\text{min}}$, and the irreducible CR background (see also the caption of Fig. 4). An MSP IC signal is injected into the mock data and subsequently a bin-by-bin fitting procedure is applied using the same background templates used in the generation of the mock data, in addition to the MSP IC and a DM IC templates. The left-hand panel shows the mean TS distribution (green solid line) and corresponding 68 per cent confidence region (green filled area) for the DM IC template. The right-hand panel displays the fraction of MSP IC (blue filled area) and DM IC (green filled area) luminosities that are obtained after injection of only the MSP IC signals of various luminosities.

whether mismodelling of the GDE could originate in a false positive detection of an MSP IC signal. This methodology is inspired by a recent study on simulated *Fermi* data by Chang et al. (2020), and a similar one performed by the CTA consortium (Acharyya et al. 2021) in the context of DM searches in the GC.

We thus repeated the same analyses performed in Sections 5.2 and 5.3, but this time, mimicking the mismodelling of the GDE as described above. We show the results, respectively, for the signal recovery test in Fig. 7, the minimum flux required for a 5σ significance detection of the MSP IC signature in Fig. 8, and lastly, the degeneracy tests between the MSPs and DM hypotheses in Fig. 9.

We found that, in the case where the Galactic diffuse background is mismodelled ('FB$_{\text{min}}$, mismodelling of the GDE' scenario), the CTA sensitivity to the MSP IC signal is reduced by approximately 38 per cent, 33 per cent, 3 per cent, 4 per cent, and 30 per cent, respectively, for the $e^{\pm}$ injection scenarios *Baseline*, *Inj1*, *Inj2*, *Inj3*, and *Inj4* (see Table 2). A summary of the minimum $L_{\gamma,\text{IC}}$ required for a CTA detection is given in Table 4.

5.5 Impact of the low-latitude FB model

We have evaluated the impact of the FBs on our sensitivity by assuming the 'FB max' model presented in Table 3 and the perfect GDE model scenario. The results of this test are presented in Figs 10, D1 (available online), and 11, which can be directly compared to Figs 4, 5, and 6, respectively.

From these comparisons, it follows that the strongest impact on the CTA sensitivity to an MSP IC signal in the GC region is due to assumptions on the FB model. We found a degradation of the sensitivity of approximately one order of magnitude at worst – which corresponds to the MSP $e^{\pm}$ injection model *Inj1* in Table 3 – and a factor of a few for the other scenarios. As in all previous cases, we summarize the minimum luminosities for detection in Table 4.

We note that in this section we have examined the degradation of the sensitivity due to uncertainties in only the FB spectrum. However, in Appendix B (available online) we also consider the case 'FB max' together with mismodelling of the GDE model. Those results confirm that uncertainties in the FB model could be the single most

challenging astrophysical background component for analyses of extended γ-ray emission with CTA in the GC region.

6 DISCUSSION AND CONCLUSIONS

6.1 Implied MSP $e^{\pm}$ injection efficiency ($f_{e^{\pm}}$) for detection with CTA

In the previous section, we investigated the ability of CTA to characterize the TeV-scale IC γ-rays produced by an unresolved population of MSPs in the Galactic bulge region. In this section, we evaluate whether the signals that can be detected by CTA are physically possible.

Using the relations presented in equations (2) and (5), and assuming that the prompt γ-ray emission from the Galactic bulge population of MSPs is fully responsible for the GCE,[9] we can obtain the minimum efficiencies $f_{e^{\pm}}$'s for a CTA detection of the MSPs' IC signal. In particular, we can convert the minimum IC luminosities (shown in Table 4) to the corresponding minimum $L_{e^{\pm}}$'s using equation (5), and then evaluate this value in equation (2), along with the inferred nominal GCE luminosity [$L_{\gamma,\text{prompt}} = 2.6 \times 10^{37}$ erg s^{-1} obtained in, e.g. Macias et al. (2019)]. However, the threshold IC luminosities presented in Table 4 are estimated in the energy range from 16 GeV to 158 TeV, while the GCE luminosity in Macias et al. (2019) was computed for $E_{\gamma} \gtrsim 700$ MeV. So, in order for us to connect the threshold IC luminosities with the $e^{\pm}$ injection luminosities that were used in our GALPROP runs, we need to extend the $e^{\pm}$ luminosity calculation to 700 MeV.[10]

---

[9]Note that analyses of the GCE (Lacroix et al. 2016) did not detect the IC signature from the putative population of MSPs in the Galactic bulge. This might be because the prompt γ-rays are much more prominent than the IC γ-rays at GeV-scale energies.

[10]This is a good approximation since the injected MSP $e^{\pm}$'s can reach roughly the same minimum energies as the γ-rays. Also, note that by comparing the $e^{\pm}$ luminosities included in GALPROP – *before propagation* – with the threshold IC luminosities, we automatically account for the effects of propagation and other energy losses (like synchrotron) for the MSP $e^{\pm}$.
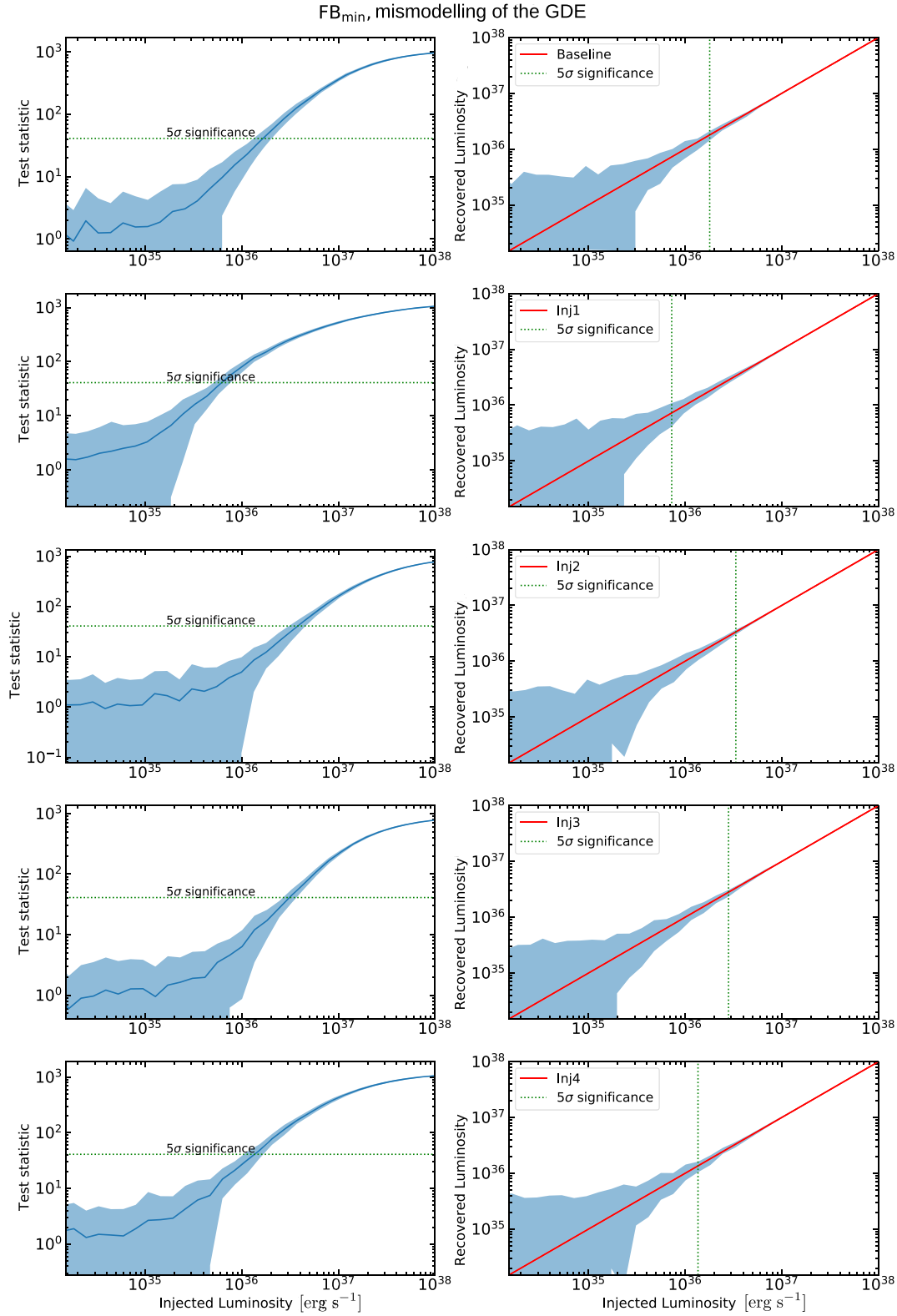
Figure 7. Same as Fig. 4, except that here we assume mismodelling of the GDE model and the FB$_{\rm min}$ model. Note that mismodelling of the GDE is mocked up by generating the data with 'GDE model 1' and then fitting the data with 'GDE model 2'.

In summary, our luminosity computations assume $E_{e^{\pm}} \geq 700$ MeV, $E\gamma \geq 700$ MeV, a distance from the Sun to the GC of 8.5 kpc (as assumed in GALPROP), and an RoI of size $10° \times 10°$ around the GC. It is useful to compare the fractional luminosities ($L_{e^{\pm}}/L_{\gamma,\rm IC}$)

predicted by GALPROP – estimated by calculating the luminosity in the GALPROP IC maps, and the $L_{e^{\pm}}$ used as input in GALPROP – so as to have a better understanding of the impact of diffusion and energy losses. We obtain that $L_{e^{\pm}}/L_{\gamma,\rm IC}$ is 21.0 for the *baseline* injection

FB$_{min}$, mismodeling of the GDE
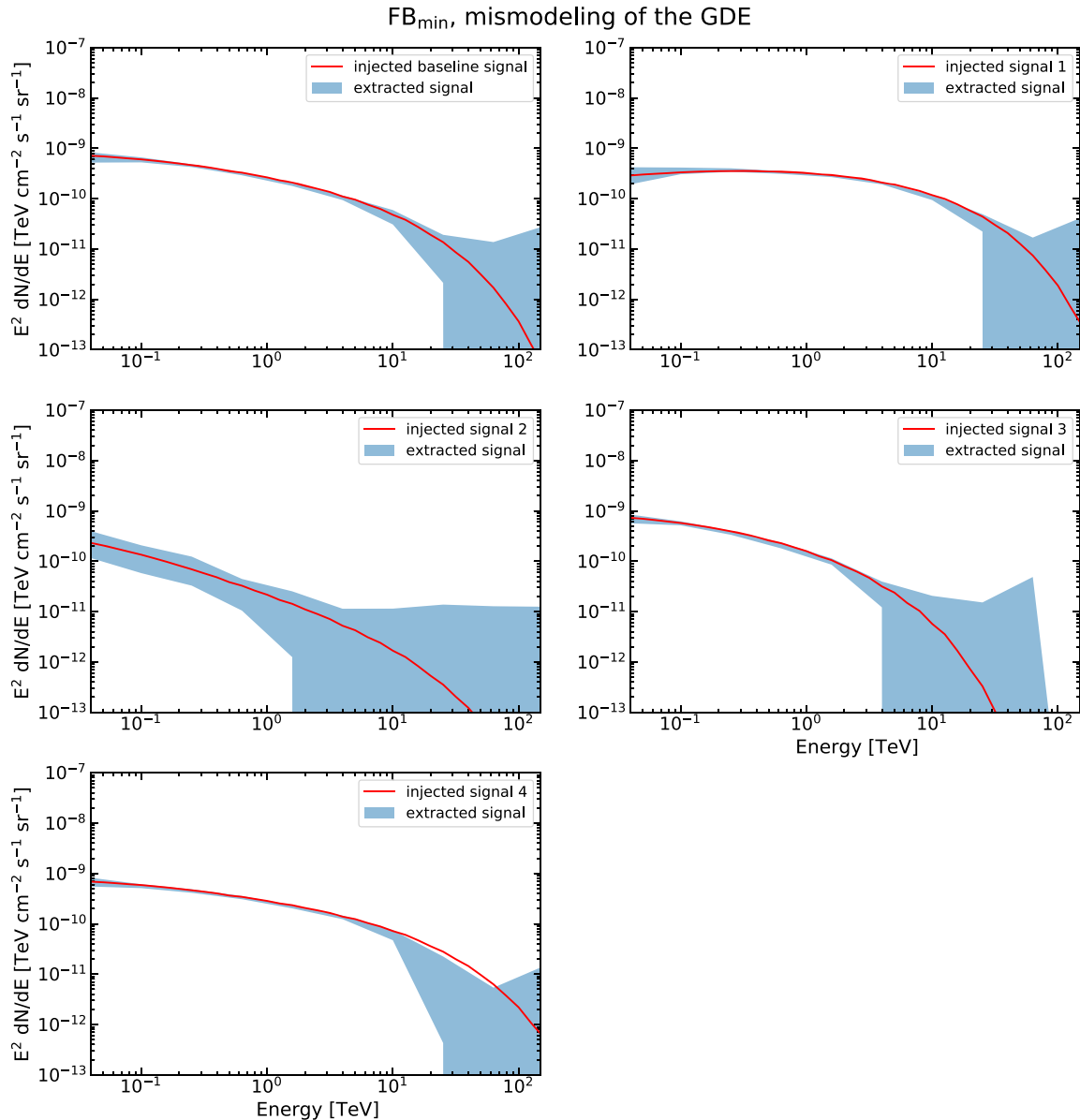
Figure 8. Same as Fig. 5, except that here we assume mismodelling of the GDE model. See also the green dotted line in Fig. 7 for the necessary IC luminosity for a 5σ significance detection of the signal.

model, 14.3 for *inj1*, 124.7 for *inj2*, 23.4 for *inj3*, and 21.1 for *inj4* (see also Table 2). The very large luminosity fraction obtained for *inj2* is explained by the fact that this injection spectrum is very soft.

Using the prescription described above, we are now able to compute the threshold $f_{e^\pm}$ values for the cases considered in our study. We show the results of this calculation in Table 5. Depending on assumptions about the astrophysical background components and the $e^\pm$ injection model, we obtain threshold $e^\pm$ efficiencies in the range $f_{e^\pm} \approx 2.9$–74.1 per cent, excluding *inj2* – which is the softest $e^\pm$ injection spectra considered in our sample. Indeed, we obtain that the $e^\pm$ luminosity needed for CTA to detect a soft spectrum like *inj2* would exceed the total budget of the MSPs' spin-down energy. This means that, if the most pessimistic GDE mismodelling scenario ('FB max' and mismodelling of the GDE) considered here is realized in nature, CTA will only be able to reliably detect the Galactic bulge population of MSPs if the overall efficiency of this population

satisfies $f_{e^\pm} \gtrsim 51.8$ per cent (see the last row of Table 5). Notice that CTA might still be suited to detect this signal with percentage-level $f_{e^\pm}$'s under some specific conditions considered in Table 5.

Interestingly, the recent study of Song et al. (2021) obtained $f_{e^\pm} \approx 10$ per cent, from a population analysis of the globular clusters of the Milky Way. Furthermore, dedicated models of MSP populations in globular clusters (Bednarek et al. 2016; Ndiyavala et al. 2018) have been recently constrained using MAGIC observations of the globular cluster M15. In particular, Acciari et al. (2019) constrained the electron efficiency to be $f_{e^\pm} \approx (0.2$–2.0) per cent, for MSPs in M15. However, very likely these strong constraints cannot be directly extrapolated to other systems containing MSPs. This is because the overall apparent efficiency in globular clusters can be strongly decreased by rapid winds from Red Clump giants in globular clusters (Bednarek et al. 2016). Note that winds can advect CR $e^\pm$ out of the globular cluster systems before they can radiate.
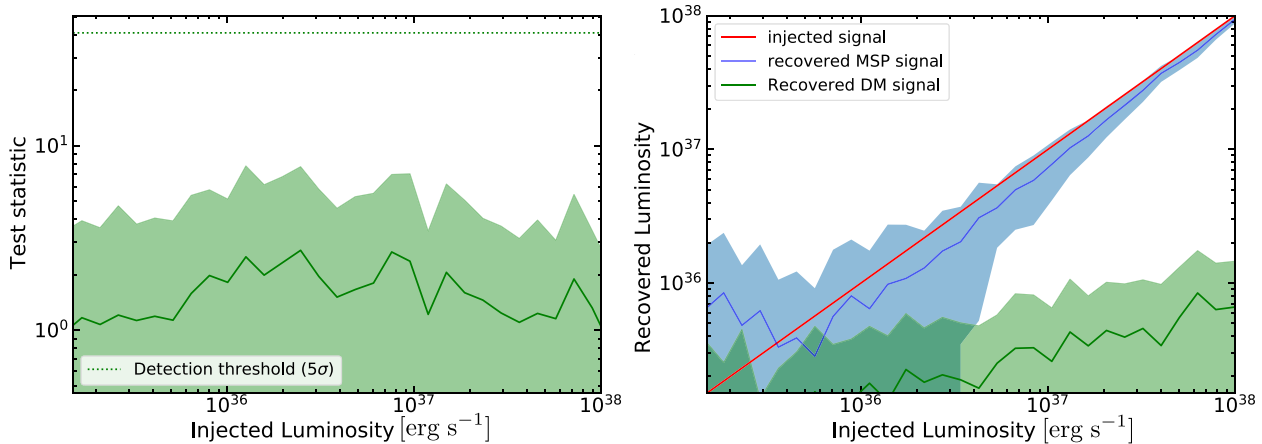
Figure 9. Same as Fig. 6, except that here we assume mismodelling of the GDE.

Additional clues about the $f_{e^\pm}$ in systems containing MSP populations have been obtained in the recent analysis by Sudoh et al. (2021). Based on the breakdown of a correlation between far-IR and radio luminosities in SFGs, Sudoh et al. (2021) posited that radio emission from MSPs could account for a large fraction of the radio luminosity observed in systems with high stellar mass and low star formation rate. This led the authors to conclude that the MSP populations in their sample of SFGs could have $f_{e^\pm}$ in excess of 90 per cent. They also noted, however, that several observational and theoretical uncertainties could lower their inferred efficiency to $f_{e^\pm} \approx 10$ per cent.

Given the above, we conclude that the efficiencies $f_{e^\pm}$ for MSPs are currently not very well constrained. In case that CTA makes an actual observation of the MSP IC signal in one of the scenarios disfavoured by our analysis, it could still be possible to reconcile such an observation with the MSP emission models. In particular, if the γ-ray emission from the Galactic bulge MSP magnetosphere is beamed, only some fraction of their prompt γ-ray luminosity can be observed from the Earth. This could decrease our inferred $f_{e^\pm}$ by a factor of a few (Sudoh et al. 2021).

In conclusion, we have demonstrated that – even under the assumption of high background uncertainties – if the $e^\pm$ injection spectra is harder than our *inj2* model (slope of dN/d$E \propto E^{-2.5}$), CTA has the potential to robustly discover the IC signal produced by a new population of MSPs in the GC. However, given observational and theoretical uncertainties on the $f_{e^\pm}$ parameter, a detection of a signal described by our *inj2* model could still be possible.

6.2 Disentangling the MSPs and DM hypotheses for the GCE

In this work, we have utilized a spatio-spectral template regression method with simulated CTA data from the GC region. In particular, we have run the signal recovery tests using a bin-by-bin analysis, which has been utilized with great success in analyses of the *Fermi*-LAT data (e.g. Ackermann et al. 2015, 2017). This methodology allows us to reduce the impact of potential biases introduced by assumptions about the spectrum of the MSPs and/or DM templates.

Using the aforementioned method, we tested whether CTA could disentangle the IC signal produced by an unresolved population of MSPs in the Galactic bulge from the one produced by a spherical distribution of DM (or a population of pulsars following a spherical

distribution). Given that the $e^\pm$ sources would follow either of these two distributions,[11] the IC maps produced by such $e^\pm$ were predicted to have discernible spatial differences in Song et al. (2019). We have injected signals of MSP IC emission with varying strengths, and then run the signal recovery pipeline including both an MSP IC template and a DM IC template in the fit. As a result, we have found that CTA has the capability of robustly disentangling these two sources, even in the presence of GDE mismodelling. Overall, we have demonstrated that if CTA discovers a diffuse IC signal under the conditions considered in Table 4, the spatial morphology of the IC signal will reveal whether it is related to stellar mass or a spherically symmetric source distribution as, for instance, would be expected for DM.

We note that TeV-scale $e^\pm$ pairs could potentially lose most of their energy very close to parent MSPs' magnetospheres. If the number of MSPs responsible for the GCE is relatively small, then the predicted IC templates could exhibit a clustering-of-photons effect (Acharyya et al. 2021), which could facilitate the detection of the MSP population in the Galactic bulge. Very promising methodologies to study these effects have been explored in the literature and include the non-Poissonian template fitting procedure (Lee et al. 2016; Leane & Slatyer 2019, 2020a, b; Chang et al. 2020; Buschmann et al. 2020), wavelet techniques (Bartels et al. 2016; Balaji et al. 2018; Zhong et al. 2020), deep learning methods (Caron et al. 2018; List et al. 2020), radio detection (Macquart & Kanekar 2015; Calore et al. 2016; Rajwade, Lorimer & Anderson 2017; Hyman et al. 2019), and X-ray detection (Berteaud et al. 2020) of point sources responsible for the Galactic bulge emission. Importantly, recent population synthesis models of MSPs (Ploeg et al. 2020) predict anywhere between 20 and 50 thousand MSPs in the Galactic bulge. We can use the selected spatial resolution of our simulations, and equations (A1), (A2), and (A3), to obtain an estimate of the number of MSPs in each spatial 3D bin of our GALPROP simulations. We find that every bin of size $200 \times 200 \times 100$ pc^3 is expected to contain $\sim$300 MSPs in the centre of the boxy bulge and $\sim$30 MSPs at 3 kpc along the long axis of the Galactic bar. Furthermore, for the nuclear bulge region we estimate $\sim$1000 in the central spatial bin. This also justifies our assumption of using a smooth density function to simulate the MSP distribution in the Galactic bulge.

---

[11]The reader is referred to Section 2.2 for details on the spatial morphologies considered in this work.
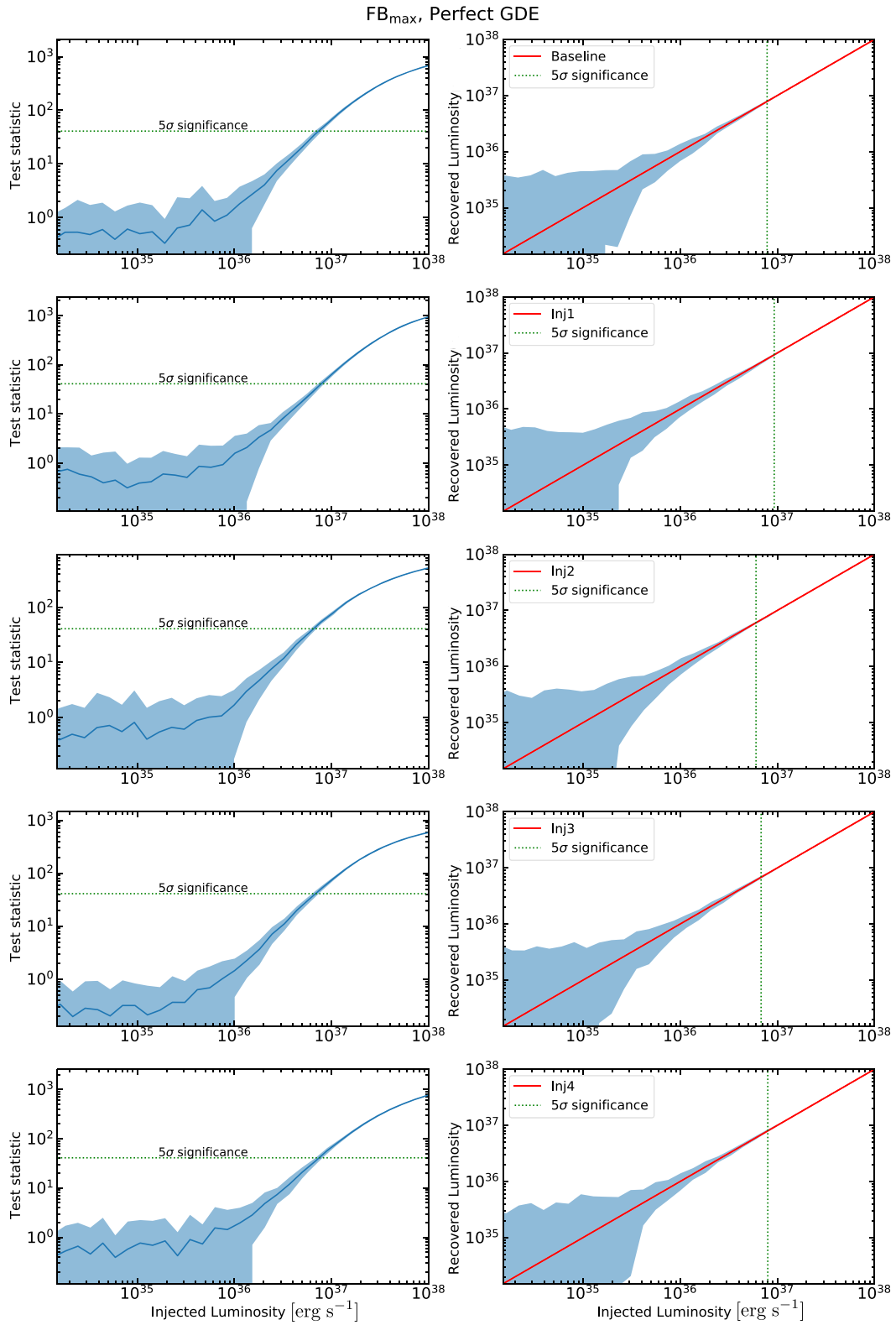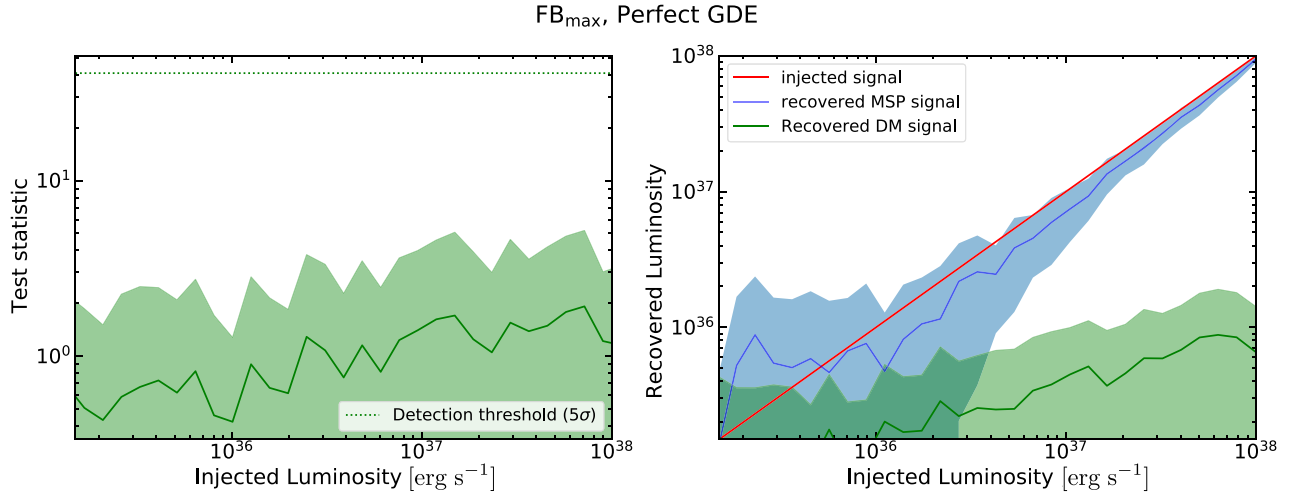
Figure 10. Same as Fig. 4, except that here we assume the FB_{max} model.

FB$_{\mathrm{max}}$, Perfect GDE

Figure 11. Same as Fig. 6, except that here we assume the FB$_{\mathrm{max}}$ model.

Table 5. Minimum MSP $e^{\pm}$ injection efficiency ($f_{e^{\pm}}$) required for a 5σ significance detection with CTA. The computation of these efficiencies uses the implied $e^{\pm}$ luminosities (see Section 6.1) based on the minimum luminosities reported in Table 4, the measured *Fermi* GeV excess γ-ray luminosity, and equation (2). The calculation of the efficiencies assumed energies greater than 700 MeV.

Baseline	Minimum $f_{e^{\pm}}$ for detection (per cent)			
	Inj1	Inj2	Inj3	Inj4
FB$_{\mathrm{min}}$, perfect GDE.				
10.5 per cent	2.9 per cent	158.4 per cent	24.3 per cent	8.2 per cent
FB$_{\mathrm{min}}$, mismodelling of the GDE.				
14.5 per cent	3.8 per cent	163.4 per cent	25.3 per cent	10.8 per cent
FB$_{\mathrm{max}}$, perfect GDE.				
57.5 per cent	41.3 per cent	259.4 per cent	55.0 per cent	58.4 per cent
FB$_{\mathrm{max}}$, mismodelling of the GDE.				
72.9 per cent	51.8 per cent	326.7 per cent	70.4 per cent	74.1 per cent

6.3 Degradation of the CTA sensitivity due to uncertainties in the astrophysical components

We have estimated the impact of various diffuse astrophysical components on the sensitivity to the signal. Using Monte Carlo simulations, we recreated a scenario in which the GDE is mismodelled, obtaining that if this scenario is realized in actual data, it will deteriorate the CTA sensitivity to the MSPs' IC signal luminosity at the $\lesssim 40$ per cent level (depending on the characteristics of the injection spectrum and assumptions about the FB model). One possible explanation as to why this effect is not larger in our analyses is that the intensity of the predicted GDE spectrum rapidly falls off with energy, becoming comparable to that of the expected MSP IC signal at TeV-scale γ-ray energies. We note that this is in stark contrast to analyses of the *Fermi*-LAT data from the GC region in which, for example, the *Fermi* GeV excess signal has an intensity that is just a small fraction of the GDE emission (e.g. Abazajian et al. 2020).

On the other hand, we observed a drastic deterioration (up to one order of magnitude) of the IC flux sensitivity when we switched from the 'FB min' model to the 'FB max' model (see Table 4). The latter was proposed in Rinchiuso et al. (2021) (see the left-hand panel of fig. 1 in that article), as a way of conservatively accounting

for the maximum γ-ray intensity that the FBs can take at the CTA energy range. This was accomplished in that work by ensuring that forthcoming measurements of diffuse γ-rays from this sky region cannot overshoot current H.E.S.S. diffuse measurements (HESS Collaboration 2016) of the GC region (inner ≈ 70 pc of the GC). As shown in Fig. 3, the 'FB max' model is the dominant astrophysical γ-ray component for energies greater than ≈ 30 GeV. This explains why the FB model produces the strongest impact on the sensitivity to the MSPs' IC signal.

Another important source of uncertainty corresponds to the spatial morphology of the FBs. The FB template assumed in our work is an inpainted version of the spatial map in Ackermann et al. (2017), which in turn was constructed using a spectral component analysis using residual γ-ray data in the 1–10 GeV range. However, the exact details of the FB map might be susceptible to the energy range that is included in the spectral component analysis of Ackermann et al. (2017). In a future study, we will address the impact of spatial uncertainties in the FB model, on the CTA sensitivity to an MSP IC signal in the GC.

6.4 Impact of the MSPs' $e^{\pm}$ injection spectrum on the sensitivity to the IC signal

As discussed in the previous section, one of the most important factors determining the characteristics of the expected IC signal corresponds to the $e^{\pm}$ injection spectrum (see also Song et al. 2019). In our analysis, we considered five different $e^{\pm}$ injection spectra, finding that these produce significantly different results. For example, the injection model *Inj1* (see Table 4) has a detection threshold luminosity that is a factor of ~ 4 lower than that of the injection model *Inj2* in both 'FB min' cases under consideration. The most likely explanation for this is that signals that mirror the spectral shape of the GDE – see the left-middle panel of Fig. 5 in comparison to the left-hand panel of Fig. 3 – are more difficult to disentangle than the signals that have a distinct spectral shape.

In Section 2.1, we presented details about our assumptions on the injection spectra of $e^{\pm}$ pairs from MSPs. Although each individual MSP – which makes up the GCE – very likely has different properties (e.g. spin-down luminosity, age, and stellar surface magnetic field), in this work we have computed the expected IC emission from MSPs by assuming a mean $e^{\pm}$ injection spectra for the whole MSP

population. This assumption is motivated by studies such as that by Kalapotharakos et al. (2019) in which, using the *Fermi*-LAT data of resolved MSPs and young pulsars, it was determined that there is a correlation between MSP γ-ray luminosity, spin-down power, spectral energy cut-off, and stellar surface magnetic field strength.

We note that in our study, the normalization of the $e^\pm$ injection spectrum is fixed by our equation (5), such that prompt γ-ray emission from the MSP population explains the GCE data. If the MSP population happened to have a rather low mean spin-down luminosity, a larger number of MSPs would be required to explain the GCE, and so our predictions would possibly not be affected. However, a lower spin-down luminosity might likely also imply a lower energy cut-off E_{cut} in equation (3). We have investigated the effect of E_{cut} with our *Inj3* and *Inj4* models. As can be seen in Tables 4 and 5, it becomes more difficult to detect the IC signal from the bulge MSP population as E_{cut} decreases. Other MSP parameters – such as pulsar age and stellar surface magnetic field – are expected to also affect the spectral slope, and the energy cut-off of the $e^\pm$ injection spectrum. The range of parameters evaluated in this work covers a generous range of possible parameters to account for these theoretical uncertainties in MSP modelling.

The modelling of the distribution of MSP $e^\pm$ throughout the Galactic bulge is based on a steady-state assumption, where the spatial distribution of MSPs is described using a smoothly varying function of position that does not change with time and the MSPs are assumed to inject $e^\pm$ at a constant rate. While in reality MSPs must have a proper motion and a certain decay time, our assumption of a continuous emission scenario is an approximation that is justified given the potentially low proper motion of MSPs (Hobbs et al. 2005) and small period derivatives ($\dot{P}$; Harding 2021). We leave for future work to explore the effect that a fully time-dependent modelling of MSPs would have in our results, but we anticipate a potentially small effect given the aforementioned arguments.

Future advances in our understanding of the MSPs' $e^\pm$ injection spectrum will help reduce the impact of this component on the sensitivity. On the theory side, future global magnetosphere simulations that include non-dipolar fields could provide a clearer picture of the $e^\pm$ injection mechanisms and predicted spectrum (Harding 2021). On the phenomenological side, multiwavelength measurements and modelling of unresolved MSPs in globular clusters (Ndiyavala et al. 2018; Song et al. 2021) and SFGs (Sudoh et al. 2021) could reveal the characteristics of the MSPs' $e^\pm$ injection spectra.

SUPPORTING INFORMATION

Supplementary data are available at *MNRAS* online.

Supplement_stab1450.pdf

Please note: Oxford University Press is not responsible for the content or functionality of any supporting materials supplied by the authors. Any queries (other than missing material) should be directed to the corresponding author for the article.

ACKNOWLEDGEMENTS

DATA AVAILABILITY

The astrophysical templates underlying this article will be shared on reasonable request to the corresponding author.

REFERENCES

Abazajian K. N., 2011, JCAP, 1103, 010
Abazajian K. N., Kaplinghat M., 2012, Phys. Rev. D, 86, 083511
Abazajian K. N., Horiuchi S., Kaplinghat M., Keeley R. E., Macias O., 2020, Phys. Rev. D, 102, 043012
Abdo A. A. et al., 2013, ApJS, 208, 17
Abdollahi S. et al., 2020, ApJS, 247, 33
Abeysekara A. U. et al., 2017, Science, 358, 911
Abramowski A. et al., 2013, A&A, 551, A26
Acciari V. A. et al., 2019, MNRAS, 484, 2876
Acero F. et al., 2016, ApJS, 223, 26
Acharya B. et al., 2018, Science with the Cherenkov Telescope Array. World Sci. Publ. Co.
Acharyya A. et al., 2021, JCAP, 01, 057
Ackermann M. et al., 2012, ApJ, 750, 3
Ackermann M. et al., 2014, ApJ, 793, 64
Ackermann M. et al., 2015, Phys. Rev. Lett., 115, 231301
Ackermann M. et al., 2017, ApJ, 840, 43
Aguilar M. et al., 2013, Phys. Rev. Lett., 110, 141102
Aharonian F. A., Atoyan A. M., Voelk H. J., 1995, A&A, 294, L41
Ajello M. et al., 2016, ApJ, 819, 44
Ajello M. et al., 2017, ApJS, 232, 18
Atoyan A. M., Aharonian F. A., Völk H. J., 1995, Phys. Rev. D, 52, 3265
Atri P. et al., 2019, MNRAS, 489, 3116
Balaji B., Cholis I., Fox P. J., McDermott S. D., 2018, Phys. Rev. D, 98, 043009
Bartels R., Krishnamurthy S., Weniger C., 2016, Phys. Rev. Lett., 116, 051102
Bartels R., Storm E., Weniger C., Calore F., 2018, Nat. Astron., 2, 819
Beck R., 2001, Space Sci. Rev., 99, 243
Bednarek W., Sitarek J., Sobczak T., 2016, MNRAS, 458, 1083
Berteaud J., Calore F., Clavel M., Serpico P. D., Dubus G., Petrucci P.-O., 2020, preprint (arXiv:2012.03580)
Buschmann M., Rodd N. L., Safdi B. R., Chang L. J., Mishra-Sharma S., Lisanti M., Macias O., 2020, Phys. Rev. D, 102, 023023
Calore F., Cholis I., Weniger C., 2015, JCAP, 03, 038
Calore F., Di Mauro M., Donato F., Hessels J. W. T., Weniger C., 2016, ApJ, 827, 143
Calore F., Donato F., Manconi S., 2021, preprint (arXiv:2102.12497)
Caron S., Gómez-Vargas G. A., Hendriks L., Ruiz de Austri R., 2018, JCAP, 05, 058
Cerutti B., Philippov A. A., Spitkovsky A., 2016, MNRAS, 457, 2401
Chang L. J., Mishra-Sharma S., Lisanti M., Buschmann M., Rodd N. L., Safdi B. R., 2020, Phys. Rev. D, 101, 023014
Coleman B., Paterson D., Gordon C., Macias O., Ploeg H., 2020, MNRAS, 495, 3350

Coronado-Blázquez J., Doro M., Sánchez-Conde M. A., Aguirre-Santaella A., 2021, Phys. Dark Univ., 32, 100845

Crocker R. M., Jones D., Melia F., Ott J., Protheroe R. J., 2010, Nature, 468, 65

Crocker R. M., Bicknell G. V., Taylor A. M., Carretti E., 2015, ApJ, 808, 107

Daylan T., Finkbeiner D. P., Hooper D., Linden T., Portillo S. K. N., Rodd N. L., Slatyer T. R., 2016, Phys. Dark Univ., 12, 1

Deil C. et al., 2017, Proc. Sci., Gammapy - A Prototype for the CTA Science Tools. SISSA, Trieste, PoS(ICRC2017)766

Delahaye T., Lavalle J., Lineros R., Donato F., Fornengo N., 2010, A&A, 524, A51

Di Mauro M., 2021, Phys. Rev. D, 103, 63029

Di Mauro M., Manconi S., Donato F., 2019, Phys. Rev. D, 100, 123015

Erber T., 1966, Rev. Mod. Phys., 38, 626

Fragione G., Antonini F., Gnedin O. Y., 2018a, MNRAS, 475, 5313

Fragione G., Pavlík V., Banerjee S., 2018b, MNRAS, 480, 4955

Freudenreich H. T., 1998, ApJ, 492, 495

Garzon F., Lopez-Corredoira M., Hammersley P., Mahoney T. J., Calbet X., Beckman J. E., 1997, ApJ, 491, L31

Gérard L., 2016, Proc. Sci., Divergent Pointing with the Cherenkov Telescope Array for Surveys and Beyond. SISSA, Trieste, PoS(ICRC2015)725

Gonthier P. L., Harding A. K., Ferrara E. C., Frederick S. E., Mohr V. E., Koh Y.-M., 2018, ApJ, 863, 199

Gordon C., Macias O., 2013, Phys. Rev. D, 88, 083521

Guépin C., Rinchiuso L., Kotera K., Moulin E., Pierog T., Silk J., 2018, J. Cosmol. Astropart. Phys., 2018, 042

Guépin C., Cerutti B., Kotera K., 2020, A&A, 635, A138

Hammersley P. L., Garzon F., Mahoney T., Lopez-Corredoira M., Torres M. A. P., 2000, MNRAS, 317, L45

Harding A. K., 2021, preprint (arXiv:2101.05751)

Hassan T. et al., 2015, Proc. Sci., Second Large Scale Monte Carlo Study for the Cherenkov Telescope Array. SISSA, Trieste, PoS(ICRC2015)971

Heiles C., 1995, in Ferrara A., McKee C. F., Heiles C., Shapiro P. R., eds, ASP Conf. Ser. Vol. 80, The Physics of the Interstellar Medium and Intergalactic Medium. Astron. Soc. Pac., San Francisco, p. 507

Herold L., Malyshev D., 2019, A&A, 625, A110

HESS Collaboration, 2016, Nature, 531, 476

Hobbs G., Lorimer D. R., Lyne A. G., Kramer M., 2005, MNRAS, 360, 974

Hooper D., Goodenough L., 2011, Phys. Lett. B, 697, 412

Hooper D., Blasi P., Serpico P. D., 2009, JCAP, 01, 025

Hooper D., Cholis I., Linden T., Fang K., 2017, Phys. Rev. D, 96, 103013

Horiuchi S., Kaplinghat M., Kwa A., 2016, JCAP, 11, 053

Hyman S. D., Frail D. A., Deneva J. S., Kassim N. E., McLaughlin M. A., Kooi J. E., Ray P. S., Polisensky E. J., 2019, ApJ, 876, 20

Ishiwata K., Macias O., Ando S., Arimoto M., 2020, JCAP, 01, 003

Jóhannsson G., Porter T. A., Moskalenko I. V., 2018, ApJ, 856, 45

Jóhannsson G., Porter T. A., Moskalenko I. V., 2019, ApJ, 879, 91

Kalapotharakos C., Harding A. K., Kazanas D., Wadiasingh Z., 2019, ApJ, 883, L4

Lacroix T., Macias O., Gordon C., Panci P., Bœhm C., Silk J., 2016, Phys. Rev. D, 93, 103004

Launhardt R., Zylka R., Mezger P., 2002, A&A, 384, 112

Leane R. K., Slatyer T. R., 2019, Phys. Rev. Lett., 123, 241101

Leane R. K., Slatyer T. R., 2020a, Phys. Rev. D, 102, 063019

Leane R. K., Slatyer T. R., 2020b, Phys. Rev. Lett., 125, 121105

Lee S. K., Lisanti M., Safdi B. R., Slatyer T. R., Xue W., 2016, Phys. Rev. Lett., 116, 051103

Linden T., Rodd N. L., Safdi B. R., Slatyer T. R., 2016, Phys. Rev. D, 94, 103013

List F., Rodd N. L., Lewis G. F., Bhat I., 2020, Phys. Rev. Lett., 125, 241102

Macias O., Gordon C., 2014, Phys. Rev. D, 89, 063515

Macias O., Gordon C., Crocker R. M., Coleman B., Paterson D., Horiuchi S., Pohl M., 2018, Nat. Astron., 2, 387

Macias O., Horiuchi S., Kaplinghat M., Gordon C., Crocker R. M., Nataf D. M., 2019, JCAP, 09, 042

Macquart J.-P., Kanekar N., 2015, ApJ, 805, 172

Michel F. C., 1991, Theoretical Astrophysics. Univ. Chicago Press, Chicago, IL

Ndiyavala H., Krüger P. P., Venter C., 2018, MNRAS, 473, 897

Ndiyavala-Davids H., Venter C., Kopp A., Backes M., 2020, MNRAS, 500, 4827

Nelder J., Mead R., 1965, Comput. J., 7, 308

Nigro C. et al., 2019, A&A, 625, A10

Pfahl E., Rappaport S., Podsiadlowski P., 2002, ApJ, 573, 283

Ploeg H., Gordon C., Crocker R., Macias O., 2017, JCAP, 1708, 015

Ploeg H., Gordon C., Crocker R., Macias O., 2020, JCAP, 12, 035

Podsiadlowski P., Pfahl E., Rappaport S., 2005, in Rasio F. A., Stairs I. H., eds, ASP Conf. Ser. Vol. 328, Binary Radio Pulsars. Astron. Soc. Pac., San Francisco, p. 327

Pohl M., Englmaier P., Bissantz N., 2008, ApJ, 677, 283

Porter T. A., Moskalenko I. V., Strong A. W., 2006, ApJ, 648, L29

Porter T. A., Jóhannsson G., Moskalenko I. V., 2017, ApJ, 846, 67

Profumo S., Reynoso-Cordova J., Kaaz N., Silverman M., 2018, Phys. Rev. D, 97, 123008

Rajwade K. M., Lorimer D. R., Anderson L. D., 2017, MNRAS, 471, 730

Rinchiuso L., Macias O., Moulin E., Rodd N. L., Slatyer T. R., 2021, Phys. Rev. D, 103, 023011

Robitaille T. P., Churchwell E., Benjamin R. A., Whitney B. A., Wood K., Babler B. L., Meade M. R., 2012, A&A, 545, A39

Silverwood H., Weniger C., Scott P., Bertone G., 2015, JCAP, 03, 055

Song D., Macias O., Horiuchi S., 2019, Phys. Rev. D, 99, 123020

Song D., Macias O., Horiuchi S., Crocker R. M., Nataf D. M., 2021, preprint (arXiv:2102.00061)

Storm E., Weniger C., Calore F., 2017, JCAP, 08, 022

Strong A. W., Moskalenko I. V., Reimer O., 2000, ApJ, 537, 763

Strong A. W., Moskalenko I. V., Ptuskin V. S., 2007, Ann. Rev. Nucl. Part. Sci., 57, 285

Sturrock P. A., 1970, Nature, 227, 465

Sturrock P. A., 1971, ApJ, 164, 529

Su M., Finkbeiner D. P., 2012, ApJ, 753, 61

Su M., Slatyer T. R., Finkbeiner D. P., 2010, ApJ, 724, 1044

Sudoh T., Linden T., Beacom J. F., 2021, Phys. Rev. D, 103, 083017

Viana A. et al., 2020, Proc. Sci., The Cherenkov Telescope Array View of the Galactic Center Region. SISSA, Trieste, PoS(ICRC2019)817

Yuan Q., Ioka K., 2015, ApJ, 802, 124

Zhong Y.-M., McDermott S. D., Cholis I., Fox P. J., 2020, Phys. Rev. Lett., 124, 231103

This paper has been typeset from a TEX/LATEX file prepared by the author.